Ho, AYQ, Perley, DA, Yao, Y, Svinkin, D, Postigo, ADU, Perley, RA, Kann, DA, Burns, E, Andreoni, I, Bellm, EC, Bissaldi, E, Bloom, JS, Brink, TG, Dekany, R, Drake, AJ, Agüí Fernández, JF, Filippenko, AV, Frederiks, D, Graham, MJ, Hristov, BA, Kasliwal, MM, Kulkarni, SR, Kumar, H, Laher, RR, Lysenko, AL, Mailyan, B, Malacaria, C, Miller, AA, Poolakkil, S, Riddle, R, Ridnaia, A, Rusholme, B, Savchenko, V, Sollerman, J, Thöne, C, Tsvetkova, A, Ulanov, M and Von Kienlin, A

 Cosmological Fast Optical Transients with the Zwicky Transient Facility: A Search for Dirty Fireballs

Article

For more information please contact researchonline@ljmu.ac.uk

CrossMark

Cosmological Fast Optical Transients with the Zwicky Transient Facility: A Search for Dirty Fireballs

Anna Y. Q. Ho[1,2,3,4], Daniel A. Perley[5], Yuhan Yao[6], Dmitry Svinkin[7], A. de Ugarte Postigo[8], R. A. Perley[9], D. Alexander Kann[10], Eric Burns[11], Igor Andreoni[12,13,14], Eric C. Bellm[15], Elisabetta Bissaldi[16,17], Joshua S. Bloom[2,3], Thomas G. Brink[2], Richard Dekany[18], Andrew J. Drake[6], José Feliciano Agüí Fernández[10], Alexei V. Filippenko[2], Dmitry Frederiks[7], Matthew J. Graham[6], Boyan A. Hristov[19], Mansi M. Kasliwal[6], S. R. Kulkarni[6], Harsh Kumar[20,*], Russ R. Laher[21], Alexandra L. Lysenko[7], Bagrat Mailyan[22], Christian Malacaria[23], A. A. Miller[24], S. Poolakkil[25,26], Reed Riddle[18], Anna Ridnaia[7], Ben Rusholme[21], Volodymyr Savchenko[27], Jesper Sollerman[28], Christina Thöne[29], Anastasia Tsvetkova[7], Mikhail Ulanov[7], and Andreas von Kienlin[30]

[1] Miller Institute for Basic Research in Science, 468 Donner Lab, Berkeley, CA, 94720, USA; annayqho@berkeley.edu
[2] Department of Astronomy, University of California, Berkeley, CA, 94720-3411, USA
[3] Lawrence Berkeley National Laboratory, 1 Cyclotron Road, MS 50B-4206, Berkeley, CA, 94720, USA
[4] Department of Astronomy, Cornell University, Ithaca, NY, 14853, USA
[5] Astrophysics Research Institute, Liverpool John Moores University, IC2, Liverpool Science Park, 146 Brownlow Hill, Liverpool, L3 5RF, UK
[6] Cahill Center for Astrophysics, California Institute of Technology, MC 249-17, 1200 E California Boulevard, Pasadena, CA, 91125, USA
[7] Ioffe Institute, 26 Politekhnicheskaya, St Petersburg, 194021, Russia
[8] Artemis, Observatoire de la Côte d'Azur, Université Côte d'Azur, CNRS, F-06304 Nice, France
[9] National Radio Astronomy Observatory, P.O. Box O, Socorro, NM, 87801, USA
[10] Instituto de Astrofísica de Andalucía (IAA-CSIC), Glorieta de la Astronomía s/n, E-18008 Granada, Spain
[11] Department of Physics & Astronomy, Louisiana State University, Baton Rouge, LA, 70803, USA
[12] Joint Space-Science Institute, University of Maryland, College Park, MD, 20742, USA
[13] Department of Astronomy, University of Maryland, College Park, MD, 20742, USA
[14] Astrophysics Science Division, NASA Goddard Space Flight Center, Mail Code 661, Greenbelt, MD, 20771, USA
[15] DIRAC Institute, Department of Astronomy, University of Washington, 3910 15th Avenue NE, Seattle, WA, 98195, USA
[16] Dipartimento di Fisica "M. Merlin" dell'Università e del Politecnico di Bari, I-70126 Bari, Italy
[17] Istituto Nazionale di Fisica Nucleare, Sezione di Bari, I-70126 Bari, Italy
[18] Caltech Optical Observatories, California Institute of Technology, Pasadena, CA, 91125, USA
[19] Center for Space Plasma and Aeronomic Research (CSPAR), University of Alabama in Huntsville, Huntsville, AL, 35899, USA
[20] Department of Physics, Indian Institute of Technology Bombay, Powai, Mumbai-400076, India
[21] IPAC, California Institute of Technology, 1200 E. California Blvd, Pasadena, CA, 91125, USA
[22] Center for Astro, Particle, and Planetary Physics, New York University Abu Dhabi, Abu Dhabi, UAE
[23] Universities Space Research Association, NSSTC, 320 Sparkman Drive, Huntsville, AL, 35805, USA
[24] Center for Interdisciplinary Exploration and Research in Astrophysics (CIERA) and Department of Physics and Astronomy, Northwestern University, 1800 Sherman Road, Evanston, IL, 60201, USA
[25] Department of Space Science, University of Alabama in Huntsville, Huntsville, AL, 35899, USA
[26] Center for Space Plasma and Aeronomic Research, University of Alabama in Huntsville, Huntsville, AL, 35899, USA
[27] ISDC, Department of Astronomy, University of Geneva, Chemin d'Ecogia, 16 CH-1290 Versoix, Switzerland
[28] The Oskar Klein Centre, Department of Astronomy, Stockholm University, AlbaNova, SE-10691 Stockholm, Sweden
[29] Astronomical Institute of the Czech Academy of Sciences (ASU-CAS), Fričova 298, 251 65 Ondřejov, CZ
[30] Max-Planck Institut für extraterrestrische Physik, D-85748 Garching, Germany

Abstract

Dirty fireballs are a hypothesized class of relativistic massive-star explosions with an initial Lorentz factor Γ_{init} below the $\Gamma_{init} \sim 100$ required to produce a long-duration gamma-ray burst (LGRB), but which could still produce optical emission resembling LGRB afterglows. Here we present the results of a search for on-axis optical afterglows using the Zwicky Transient Facility (ZTF). Our search yielded seven optical transients that resemble on-axis LGRB afterglows in terms of their red colors ($g - r > 0$ mag), faint host galaxies ($r > 23$ mag), rapid fading ($dr/dt > 1$ mag day^{-1}), and in some cases X-ray and radio emission. Spectroscopy of the transient emission within a few days of discovery established cosmological distances (redshift $z = 0.876$ to 2.9) for six of the seven events, tripling the number of afterglows with redshift measurements discovered by optical surveys without a γ-ray trigger. A likely associated LGRB (GRB 200524A, GRB 210204A, GRB 210212B, and GRB 210610B) was identified for four events (ZTF 20abbiixp/ AT 2020kym, ZTF 21aagwbjr/AT 2021buv, ZTF 21aakruew/AT 2021cwd, and ZTF 21abfmpwn/AT 2021qbd) post facto, while three (ZTF 20aajnksq/AT 2020blt, ZTF 21aaeyldq/AT 2021any, and ZTF 21aayokph/AT 2021lfa) had no detected LGRB counterpart. The simplest explanation for the three "orphan" events is that they were regular LGRBs missed by high-energy satellites owing to detector sensitivity and duty cycle, although it is possible that they were intrinsically subluminous in γ-rays or viewed slightly off-axis. We rule out a scenario in which dirty fireballs have a

---

* LSSTC Data Science Fellow 2018.

similar energy per solid angle to LGRBs and are an order of magnitude more common. In addition, we set the first direct constraint on the ratio of the opening angles of the material producing γ-rays and the material producing early optical afterglow emission, finding that they must be comparable.

Unified Astronomy Thesaurus concepts: Gamma-ray bursts (629); Transient sources (1851); High energy astrophysics (739); Time domain astronomy (2109)

1. Introduction

Decades of observations of long-duration γ-ray bursts (LGRBs) and their associated afterglows have revealed that in the deaths of some massive ($M > 10\,M_\odot$) stripped-envelope stars, the newborn compact object can couple 10^{51} erg of energy to ultrarelativistic (initial Lorentz factor $\Gamma_{\rm init} \gg 100$) material, and that this phenomenon preferentially occurs in low-metallicity environments (Kouveliotou et al. 2012). In the traditional LGRB model (Piran 2004; Mészáros 2006; Kumar & Zhang 2015), the outflow is collimated into a jet a few degrees wide as it tunnels through the star. Viewed on-axis, the observer sees a seconds-long burst of γ-rays from collisions within the jet, then emission from X-ray to radio wavelengths called the "afterglow" (Mészáros & Rees 1997; Sari et al. 1998; van Paradijs et al. 2000; Panaitescu & Kumar 2002; Greiner et al. 2011) on timescales of minutes to years. Thousands of afterglows have been detected to date[31], almost all in targeted follow-up observations of discoveries by GRB satellites such as the High Energy Transient Explorer 2 (HETE-2; Ricker et al. 2003), Fermi (Meegan et al. 2009), and the Neil Gehrels Swift Observatory (Gehrels et al. 2004).

Despite the significant progress made by LGRB discoveries, many important questions cannot be answered by relying on existing γ-ray satellites to discover relativistic outflows from collapsing stars. In particular, the rate and angular structure of LGRB jets are unknown in large part because observed LGRBs are viewed almost entirely on-axis (or close to on-axis; Ryan et al. 2015), with only a few suggested exceptions (Huang et al. 2004; Ramirez-Ruiz et al. 2005; Butler et al. 2005; Krühler et al. 2009). Relatedly, it is unknown whether ultrarelativistic speeds, which can only be attained with very small amounts of matter entrained in the jet ("low mass-loading"), are central to the phenomenon. It has been hypothesized that mass-loaded jets ("dirty fireballs;" Paczyński 1998; Dermer et al. 1999) are more common (Huang et al. 2002), but have gone unnoticed because their emission peaks at energies below the range of existing γ-ray detectors (Dermer et al. 1999), instead appearing as X-ray flashes (Heise et al. 2001; Zhang et al. 2004; Sakamoto et al. 2005; Soderberg et al. 2007).

A promising approach to answering the above questions is to find relativistic outflows via their afterglow emission, without relying on a trigger from a γ-ray satellite. Assuming that dirty fireballs result in successful relativistic outflows with a similar energy per solid angle to those of LGRBs, they should produce luminous and rapidly fading optical afterglows (Huang et al. 2002; Rhoads 2003). The afterglows from clean or dirty fireballs viewed off-axis ($\theta_{\rm obs} > 1/\Gamma_{\rm init}$) will eventually become visible to the observer as the jet decelerates and expands sideways, often referred to as "orphan" afterglows (Rhoads 1997; Perna & Loeb 1998; Dalal et al. 2002; Granot et al. 2002; Nakar et al. 2002; Totani & Panaitescu 2002). For a structured jet (see Granot & Ramirez-Ruiz 2010 for an overview), orphan afterglows could also be detected from jets viewed within the

initial opening angle of relativistic material, but outside the narrow high-Lorentz factor region emitting γ-rays; such events have been referred to as "on-axis orphans" (Nakar & Piran 2003).

Finding optical afterglows without a GRB trigger is a longstanding goal of transient surveys, and prior to the Zwicky Transient Facility (ZTF; Bellm et al. 2019b; Graham et al. 2019) had only been achieved three times. Searches at X-ray (Grindlay 1999; Greiner et al. 2000; Khabibullin et al. 2012), optical (Rau et al. 2006; Berger et al. 2013; Ho et al. 2018; Huang et al. 2020), and radio (Levinson et al. 2002; Gal-Yam et al. 2006) wavelengths have to contend with a large false-positive rate, particularly from stellar flares at optical and X-ray wavelengths, and from active galactic nuclei (AGNs) at radio wavelengths. Nonetheless, two confirmed optical afterglows were serendipitously discovered via fading broadband after-glow emission: iPTF14yb (Cenko et al. 2015) and ATLAS17-aeu (Stalder et al. 2017; Bhalerao et al. 2017; Melandri et al. 2019) were discovered by the Palomar Transient Factory (Law et al. 2009) and the ATLAS survey (Tonry et al. 2018), respectively, with LGRB counterparts discovered post facto. A third optical event, PTF11agg (Cenko et al. 2013), resembled a GRB afterglow (rapidly fading optical emission, a long-lived scintillating radio counterpart, coincidence with a dwarf galaxy) yet had no identified high-energy counterpart, leading to suggestions that it might be a dirty fireball. At radio wavelengths, a promising candidate off-axis afterglow has been identified in VLA Sky Survey data (Law et al. 2018; Mooley et al. 2022).

In the last few years, with the enhanced survey speed (Bellm 2016; Ofek & Ben-Ami 2020) of ZTF, the discovery of optical afterglows without a GRB trigger has become routine. As we discuss in this paper, ten afterglows have been discovered to date using ZTF data, five from the year 2021 alone. Most were identified by human scanners within 12 hr of the first ZTF detection, through dedicated searches for fast optical transients that make use of the transient's rise rate, fade rate, color, and contextual information such as the host galaxy (Ho et al. 2020a; Andreoni et al. 2020a, 2021). Searches for very fast ($\ll 30\,{\rm s}$) optical transients accompanying fast radio bursts have also been conducted using ZTF data (Andreoni et al. 2020b).

In this paper we present discovery and follow-up details for six of the ten ZTF afterglows (AT 2020kym, AT 2021any, AT 2021buv, AT 2021cwd, AT 2021lfa, and AT 2021qbd), including two (AT 2021any and AT 2021lfa) with no detected GRB counterpart. We also present deep imaging with Keck at the position of the ZTF afterglow AT 2020blt, the discovery of which was published by Ho et al. (2020b). We do not present new data on the remaining three afterglows, two of which (AT 2020sev and AT 2020yxz) had detected GRB counterparts and were published by Andreoni et al. (2021), and one of which (AT 2019pim) had no GRB counterpart and will be published separately (D. Perley et al. in preparation). We describe our search strategy and give an overview of the sample

---

[31] https://www.mpe.mpg.de/~jcg/grbgen.html

in Section 2. In Section 3 we compare the multiwavelength properties of the ZTF afterglows to the cosmological LGRB population. Section 4 discusses the implications for dirty fireballs, jet collimation, and the prevalence of relativistic jets in collapsing massive stars. We summarize in Section 5 and discuss how to make future progress.

Throughout the paper we use the term "afterglow" to refer to cosmological fast optical transients whose observed properties strongly resemble those of GRB afterglows. In addition, for brevity we use the term "orphan afterglow" to refer to afterglows with no associated detected GRB. However, as discussed in Section 3.2, an associated LGRB cannot be ruled out, so a more precise term would be "apparently orphan." We use "on-axis" to refer to a viewing angle that is within the opening angle of the initial relativistic material.

We assume a flat ΛCDM cosmology with $H_0 = 67.7 \, \mathrm{km \, s^{-1} \, Mpc^{-1}}$ and $\Omega_M = 0.307$ (Planck Collaboration et al. 2016). Times are presented in UTC, and magnitudes are given in AB (Oke & Gunn 1983). The optical photometry and spectroscopy will be made public through WISeREP, the Weizmann Interactive Supernova Data Repository (Yaron & Gal-Yam 2012).

2. Observations

2.1. ZTF

The ZTF custom mosaic camera (Dekany et al. 2020) is mounted on the 48 inch Samuel Oschin Telescope (P48) at Palomar Observatory. As summarized by Bellm et al. (2019a), during Phase I (ZTF-I; 2018–2020) observing time was divided between public (40%), partnership (40%), and Caltech (20%) surveys. During Phase II (ZTF-II; 2020–present) the survey data is 50% public and 30% partnership. Three custom filters are used (g_{ZTF}, r_{ZTF}, and i_{ZTF}; hereafter g, r, and i, respectively; Dekany et al. 2020) and images reach a typical dark-time limiting magnitude of $r \approx 20.5$ mag.

Images are processed and reference-subtracted by the IPAC ZTF pipeline (Masci et al. 2019) using the Zackay et al. (2016) image-subtraction algorithm. Every 5σ point-source detection is saved as an "alert." Alerts are distributed in Avro format (Patterson et al. 2019) and can be filtered based on a machine-learning real–bogus metric (Mahabal et al. 2019; Duev et al. 2019); host-galaxy characteristics, including a star–galaxy classifier (Tachibana & Miller 2018); and light-curve properties. During ZTF-I the collaboration used a web-based system called the GROWTH marshal (Kasliwal et al. 2019) to identify, monitor, and coordinate follow-up observations for transients of interest. In ZTF-II the collaboration uses the Fritz marshal (van der Walt et al. 2019; Duev et al. 2019).

The ten afterglows discovered to date by ZTF were identified by several different surveys. Four events were discovered as part of high-cadence (HC) observations—either the HC partnership survey, which covered 2500 deg^2 with six visits per night (three in r band and three in g band), or the ZTF Uniform Depth Survey (ZUDS[32]), which covered 2500 deg^2 with six visits per night (2r, 2g, and 2i). Three events were discovered in gr one-day cadence data, including two from public observations shadowing the Transiting Exoplanet Survey Satellite (TESS; Ricker et al. 2014) fields (van Roestel et al. 2019). Finally, two events were discovered as part of the

public ZTF-II all-sky survey, which covers 15,000 deg^2 in r band and g band every two nights. An additional afterglow (AT 2019pim; D. Perley et al., in preparation) was identified in follow-up observations to a gravitational-wave trigger (Kasliwal et al. 2020).

2.2. Search Procedure

Every night, the ZTF alert stream is filtered by several independent pipelines to identify young or fast-evolving transients. In this paper we focus on events discovered via the approach described by Ho et al. (2020a) and Perley et al. (2021b). In short, basic cuts are applied to remove artifacts, asteroids, and stellar flares. Remaining transients are divided into several groups, including new transients (those with no detections prior to the current night). One of us (A.Y.Q.H., D.A.P., or Y.Y.) visually inspects the new transients and determines whether any meet the following criteria for afterglows.

1. A fast rise from the previous nondetection ($\gtrsim 0.5$ mag day^{-1}).
2. Red colors ($g - r > 0$ mag) expected from optically thin synchrotron radiation (see Ho et al. 2020a) *or* rapid intranight fading in a single band.
3. Either no, or a very faint, associated host in deep archival imaging from the Legacy Survey (Dey et al. 2019) or Pan-STARRS1 (Chambers et al. 2016).

The criteria listed above were designed to identify on-axis afterglows with high confidence, because our scientific focus is on dirty fireballs. Off-axis afterglows might rise more slowly and therefore not pass our cuts (van Eerten et al. 2010). We defer a discussion of search criteria for off-axis afterglows to future work. In addition, we expect to miss afterglows that are first detected late in their evolution; this is better suited to filters based solely on transient decay rate, such as ZTFReST (Andreoni et al. 2020a, 2021).

Our search criteria evolved over time. Based on a strategy developed to discover afterglows in iPTF data (Ho et al. 2018), we initially searched for afterglows via rapid intranight fading. However, the intranight-fading approach has two limitations: it requires multiple observations per night in a single filter, and ZTF only obtains HC observations across a few thousand square degrees of sky. In addition, when an afterglow is discovered it has already faded significantly, making spectroscopic follow-up observations more difficult. To discover afterglows earlier in their evolution and over a wider area of sky, we broadened our strategy to include also events that rapidly brighten (Ho et al. 2020a). This approach enabled us to discover two events in the two-day cadence all-sky public survey (AT 2021cwd and AT 2021lfa) that showed no significant fading in the ZTF data: in fact, each event had only one g-band and one r-band measurement in the alert stream. We discuss the possibilities enabled by discovering afterglows in the all-sky survey in Section 5.

After a candidate is identified by the daily scanner, we check for associated GRBs, obtain follow-up observations to confirm the afterglow nature, and publicly announce the discovery of the transient. In most cases, we obtain deep imaging to measure the rate of fading and obtain a better constraint on the color. We primarily use the Liverpool Telescope (LT; Steele et al. 2004) owing to its sensitivity, robotic scheduling, and multiband capabilities. When LT is unavailable, we request observations with the Spectral Energy Distribution Machine (SEDM; Blagorodnova et al. 2018; Rigault et al. 2019) on the Palomar 60 inch

---

Table 1
Summary of Cosmological Fast Transients Discovered by Optical Surveys to Date

Name	R.A. (J2000)	Decl. (J2000)	IAU Name	Discovery Date (MJD)	Discovery Mag. (AB)	Redshift	GRB	Ref.
PTF11agg	08:22:17.195	+21:37:38.26	⋯	55591.2203	$R = 18.26 \pm 0.05$	$0.5 \lesssim z \lesssim 3.0$	⋯	[1]
iPTF14yb	14:45:58.01	+14:59:35.1	⋯	56714.4289	$r' = 18.16 \pm 0.03$	1.9733	140226A	[2]
ATLAS17aeu	09:13:13.89	+61:05:33.6	⋯	57758.4130	$i_{P1} = 17.75 \pm 0.01$	$1 \lesssim z \lesssim 2.9$	170105A	[3,4,5]
ZTF19abvizsw	18:37:53.48	+61:29:52.7	AT 2019pim	58728.1799	$g = 20.04 \pm 0.16$	1.2596	⋯	[6,7]
ZTF20aajnksq	12:47:04.87	+45:12:02.3	AT 2020blt	58876.2801	$r = 19.57 \pm 0.14$	2.9	⋯	this work;[a] [8]
ZTF20abbiixp	14:12:10.33	+60:54:19.0	AT 2020kym	58993.2863	$r = 17.35 \pm 0.04$	1.256	200524A	this work; [9,10]
ZTF20abtxwfx	16:41:21.21	+57:08:20.5	AT 2020sev	59079.2220	$r = 19.27 \pm 0.10$	Unknown	200817A	[10]
ZTF20acozryr	02:48:44.31	+12:08:14.1	AT 2020yxz	59157.3661	$g = 19.47 \pm 0.19$	1.105	201103B	[10]
ZTF21aaeyldq	08:15:15.33	−05:52:01.3	AT 2021any	59230.2916	$r = 17.92 \pm 0.06$	2.5131	⋯	this work; [11]
ZTF21aagwbjr	07:48:19.32	+11:24:34.1	AT 2021buv	59249.2966	$r = 17.11 \pm 0.05$	0.876	210204A	this work; [10]
ZTF21aakruew	10:24:42.15	+11:36:40.9	AT 2021cwd	59257.3697	$g = 19.57 \pm 0.21$	Unknown	210212B	this work; [12]
ZTF21aayokph	12:32:48.72	−01:29:22.5	AT 2021lfa	59338.2325	$r = 18.60 \pm 0.08$	1.0624	⋯	this work; [13]
ZTF21abfmpwn	16:15:40.38	+14:23:56.5	AT 2021qbd	59376.2325	$g = 18.49 \pm 0.10$	1.1345	210610B	this work;[14]

Notes.
[a] "This work" means we provide discovery and/or follow-up data as part of this paper.

References. [1] Cenko et al. (2013), [2] Cenko et al. (2015), [3] Stalder et al. (2017), [4] Bhalerao et al. (2017), [5] Melandri et al. (2019), [6] Perley et al. (2019a), [7] Kasliwal et al. (2020), [8] Ho et al. (2020a), [9] Ho et al. (2020c), [10] Andreoni et al. (2021), [11] Ho et al. (2021b), [12] Yao et al. (2021c), [13] Yao et al. (2021b), and [14] Perley et al. (2021d).

telescope (P60; Cenko et al. 2006a) or the Growth-India Telescope (GIT). The latency from the first ZTF detection to the first epoch of follow-up imaging has ranged from 0.2 days to 0.9 days. For identifying an associated detected GRB, we search the archives of the third Interplanetary Network (IPN[33]), which consists of ten spacecraft that provide all-sky full-time monitoring for high-energy bursts. The most sensitive GRB detectors in the IPN are the Burst Alert Telescope (BAT; Barthelmy et al. 2005) onboard the Neil Gehrels Swift Observatory (Swift; Gehrels et al. 2004), the Gamma-ray Burst Monitor (GBM; Meegan et al. 2009) on the Fermi spacecraft, and the KONUS instrument on the Wind spacecraft (Konus-Wind; Aptekar et al. 1995). If a transient is confirmed to be rapidly fading, and has colors consistent with optically thin synchrotron radiation, we trigger X-ray observations with Swift and optical spectroscopy of the transient emission to measure its redshift. If a candidate is confirmed to be cosmological and is orphan (no GRB is found post facto), we trigger radio observations with the Very Large Array (VLA; Perley et al. 2011). The time from first ZTF detection to public announcement is typically 24 hr.

2.3. Overview of ZTF Afterglows

The search procedure outlined in Section 2.2 has resulted in the discovery of seven afterglows to date. In this paper we present Keck imaging at the position of the previously published afterglow AT 2020blt (Ho et al. 2020b), as well as discovery and follow-up details for the six afterglows discovered after AT 2020blt. Three additional afterglows have been discovered by ZTF (Andreoni et al. 2020a, 2021; D. Perley et al. 2022, in preparation) and we do not present any new data on these objects in this paper.

Table 1 summarizes all fast optical transients discovered by optical transient surveys that were classified as afterglows based either on the post-facto detection of a likely GRB counterpart, or confirmation of relativistic ejecta from a redshift measurement or radio observations. With ZTF, the number of optically discovered afterglows has increased from three

(of which two had redshift measurements) to 13 (of which nine have redshift measurements).

The afterglows in Table 1 constitute the shortest-lived optical extragalactic transients that have been discovered in optical survey data and followed up in real time. To illustrate this, Figure 1 shows the duration above half-maximum intensity and the peak absolute magnitude for optical transients, primarily with light curves observed by ZTF (Fremling et al. 2020; Perley et al. 2020; Ho et al. 2021c). Most supernovae (SNe) evolve on timescales from 10 to 100 days, powered by radioactive decay, with their characteristic duration set by diffusion through optically thick ejecta (Villar et al. 2017a). By contrast, afterglow emission is governed by optically thin synchrotron radiation. We caution that for the afterglows, estimates of the duration and peak luminosity are imprecise because the ZTF cadence is much slower than the light-curve timescale; the exception is AT 2019pim owing to TESS observations of the light curve (D. Perley et al., in preparation; Fausnaugh et al. 2019). To estimate the duration, we use best-fit power laws to the light curve (Section 3.2). The luminosity estimates are described in Section 3.3.

In the remainder of this section we provide discovery and follow-up details for events discovered by our search procedure. The X-ray, optical, and radio light curves are respectively provided in Tables 6, 7, and 8 in the Appendix. When appropriate, we estimate the chance spatial and temporal coincidence of the optical transient with a GRB, by calculating the number of LGRBs we expect a given facility to detect in the localization region during the time interval of interest. For Fermi-GBM, we use the fact that during the year 2020 GBM detected 260 bursts, for a rate of 0.7 day^{-1}. For the IPN, we use the fact that according to the IPN master list,[34] during the year 2020 IPN detected 422 bursts, an average of 1.5 day^{-1}.

2.3.1. ZTF 20abbiixp/AT 2020kym/GRB 200524A

ZTF 20abbiixp was first detected by ZTF on 2020 May 24.29 (MJD 58993.29) in an r-band image at $r = 17.35 \pm 0.04$ mag as
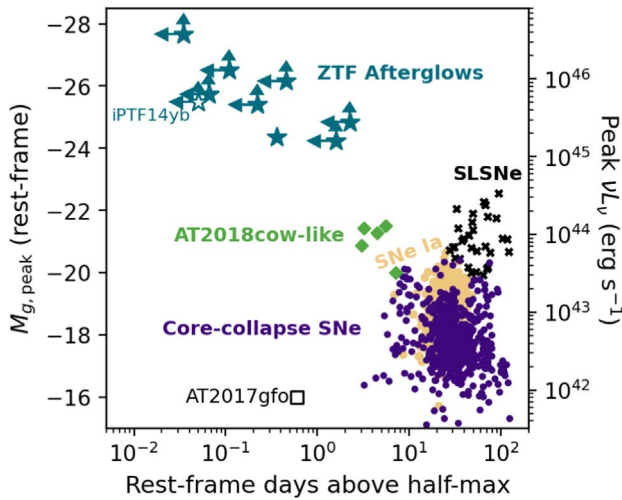

Figure 1. The duration and luminosity of optical transients. Measurements of superluminous supernovae (SLSNe), Type Ia supernovae (SNe Ia), and most core-collapse supernovae (CC SNe) are from the ZTF Bright Transient Survey (Fremling et al. 2020; Perley et al. 2020). Measurements of short-duration CC SNe and AT 2018cow-like transients are from dedicated searches for fast-evolving transients (Prentice et al. 2018; Perley et al. 2019b, 2021b; Ho et al. 2020b, 2021c; Yao et al. 2022). For reference we also show the timescale and luminosity of the optical emission from GW170817/AT 2017gfo (Coulter et al. 2017; Cowperthwaite et al. 2017; Kasliwal et al. 2017; Drout et al. 2017; Villar et al. 2017b) and of iPTF14yb (the only optically discovered afterglow prior to ZTF with a redshift measurement; Cenko et al. 2015). The afterglows discussed in this paper are the fastest and most luminous optical transients discovered and monitored in real time. Owing to the cadence of ZTF, our measurements typically represent upper limits on the duration and lower limits on the peak luminosity. Measurements are in rest-frame g band when possible, with a crude K-correction applied (Equation (1) for afterglows; see Ho et al. (2021c) for other sources).

part of the ZUDS. The most recent nondetection was 0.84 day prior at $g > 20.51$ mag. The most recent r-band nondetection was 1.01 days prior at $r > 20.79$ mag, giving an r-band rise rate of >3.4 mag day^{-1}.

There were five detections the first night, all in r band, which showed significant fading of 0.35 mag over 0.48 hr (18 mag day^{-1}); we provide the full set of ZTF photometry in Table 6, and plot the r-band light curve in Figure 2. Legacy Survey pre-imaging (Dey et al. 2019) showed no associated host at the transient position down to $g \approx r \approx 24$ mag. The fast rise, rapid intranight fading, and lack of detected host in deep imaging led the transient to be flagged by the daily scanner on 2020 May 24.8. ZTF 20abbiixp also passed the ZTFReST search criteria during the pipeline's science-validation period (Andreoni et al. 2021).

A post facto search for an associated GRB identified the long-duration GRB 200524A (Pookalil et al. 2020; Fana Dirirsa et al. 2020) consistent with the position and time of ZTF 20abbiixp. GRB 200524A had triggered the Fermi-GBM and the Fermi-Large Area Telescope (LAT; Atwood et al. 2009), and Swift X-ray Telescope (XRT; Burrows et al. 2005) Target-of-Opportunity (ToO) observations had been initiated (Evans & Swift Team 2020). The burst was found to have also triggered ASTROSAT (Gupta et al. 2020; Singh et al. 2014) and Konus-Wind (Svinkin et al. 2020).

The trigger time was 1.8 hr prior to the first ZTF detection. The offset was 0°.151 from the LAT position, which had a localization region of radius 0°.2 (90% containment, statistical error only). The expected number of GRBs detected by GBM in this location over a 0.84 days window is $R_{GBM} \times 0.84$ days $\times (\pi(0.2)^2)/41253 = 2 \times 10^{-6}$. We therefore consider the association secure. We

publicly reported the transient (Ho et al. 2020c) and saved it to the Transient Name Server (TNS[35]), where it was assigned the name AT 2020kym. Our public report of the ZTF transient and likely GRB association represented the first identification of the afterglow of GRB 200524A.

GRBs detected by Fermi-LAT are of general interest because they typically have a relativistic energy release that is an order of magnitude or more greater than the canonical 10^{51} erg value, as well as brighter-than-average X-ray and optical afterglows (Nysewander et al. 2009; Cenko et al. 2011; McBreen et al. 2010). A multiwavelength analysis of AT 2020kym will be published in a separate paper by A. Ghosh et al. (in preparation), so here we simply summarize the observations that we and other groups obtained.

We obtained a long-slit spectrum of AT 2020kym between $\Delta t = 26.6$ hr and $\Delta t = 27.8$ hr with the Gemini Multi-Object Spectrograph (GMOS) on Gemini-North (Hook et al. 2004) under our ToO program[36], and as discussed by Yao et al. (2021a), measured a redshift of $z = 1.256$. The spectrum will be published by A. Ghosh et al. (in preparation).

Because of the interest in Fermi-LAT GRBs, a variety of follow-up observations were obtained for this event. We triggered our VLA program[37] beginning 5 days after the burst and obtained several observations at 10 GHz, which will be presented by A. Ghosh et al. (in preparation). The X-ray afterglow was detected by Swift-XRT (Capalbi et al. 2020). Optical photometry was obtained with a large number of facilities (Kumar et al. 2020b; Lipunov et al. 2020; Rumyantsev et al. 2020; Sanwal et al. 2020; Belkin et al. 2020; Izzo 2020; Perley & Ho 2020; de Ugarte Postigo et al. 2020; Hosokawa et al. 2020; Kumar et al. 2020a; Zheng et al. 2020; Blazek et al. 2020; Kuin et al. 2020).

2.3.2. ZTF 21aaeyldq/AT 2021any

ZTF 21aaeyldq was first detected by ZTF on 2021 January 16.29 (MJD 59230.29) in an r-band image at $r = 17.92 \pm 0.06$ mag as part of the HC partnership survey. The most recent nondetection was 20.3 minutes prior at $r > 20.28$ mag (in a public-data image), giving a rise rate of > 167 mag day^{-1}. There were six detections the first night in r band and g band, which showed significant fading of 1.9 mag over 3.3 hr (14 mag day^{-1}) and an extinction-corrected red color of $g - r = (0.25 \pm 0.19)$ mag. The ZTF photometry is presented in Table 6, the g- and r-band light curves are shown in Figure 3, and the r-band light curve is shown compared to other events in the right panel of Figure 2. No host galaxy was visible at the transient position in deep Legacy Survey pre-imaging (>24 mag). Owing to the fast fading, red color, and lack of detected host, the transient was flagged by the daily scanner on 2021 January 16.75.

We searched the Fermi-GBM Burst Catalog[38], the Fermi-GBM Subthreshold Trigger list[39] (with reliability flag not equal to 2), the Swift GRB Archive[40], and the Gamma-Ray Coordinates Network archives[41] for an associated GRB between the last ZTF nondetection (2021 January 16.28) and the first ZTF

---

[35] https://www.wis-tns.org/
[36] GN-2020A-Q-117; PI: Miller
[37] Project ID VLA/20A-374; PI A. Ho
[38] https://heasarc.gsfc.nasa.gov/W3Browse/fermi/fermigbrst.html
[39] https://gcn.gsfc.nasa.gov/fermi_gbm_subthresh_archive.html
[40] https://swift.gsfc.nasa.gov/archive/grb_table/
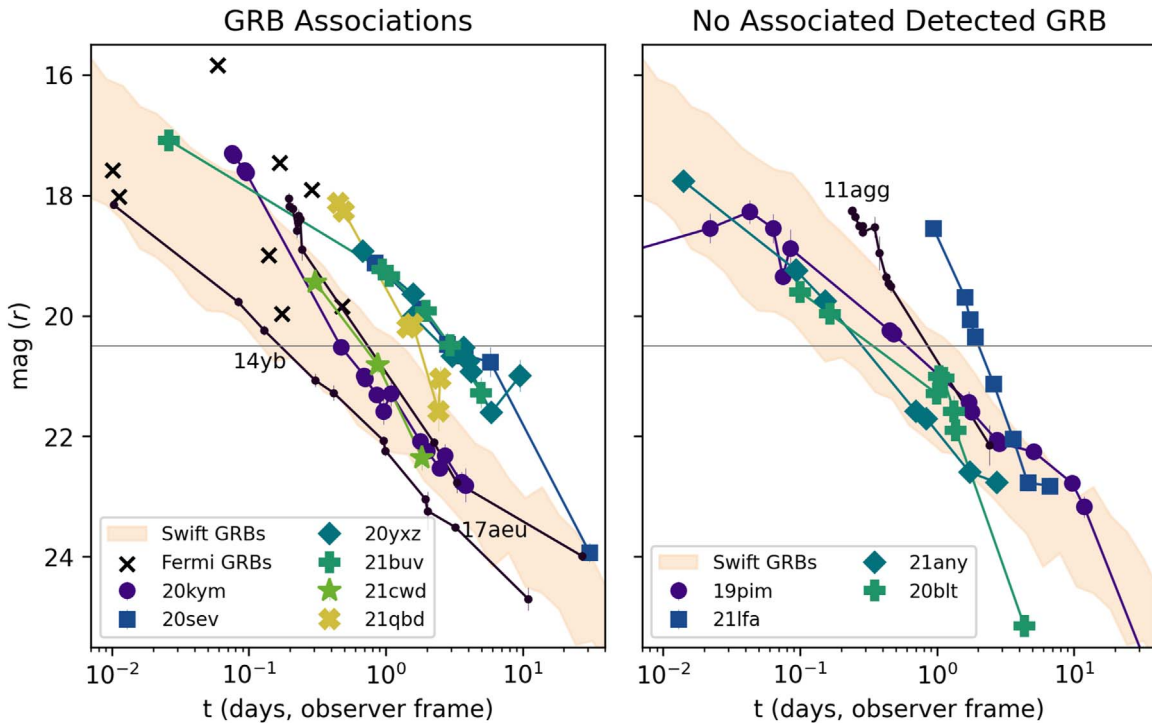[41] https://gcn.gsfc.nasa.gov/gcn3_archive.html

Figure 2. The r-band light curve (corrected for Milky Way extinction) of each ZTF afterglow compared to the sample of afterglows detected in follow-up observations to Swift-BAT triggers (Kann et al. 2010) and Fermi-GBM triggers (Singer et al. 2015). The left panel shows afterglows with associated detected GRBs, and the right panel indicates afterglows with no associated detected GRB. For the orphan events, we caution that the estimated t_0 is uncertain. The shaded region corresponds to the 25–75 percentile bounds of the Swift-BAT sample (Kann et al. 2010). The crosses indicate the first detection of each Fermi-GBM afterglow in Singer et al. (2015). The horizontal gray line indicates the nominal ZTF limit of 20.5 mag. Photometry is obtained from Cenko et al. (2013, 2015), Bhalerao et al. (2017), Ho et al. (2020a), Andreoni et al. (2021), and D. Perley et al. (2022, in preparation). For ATLAS17aeu we include c-band points. For AT 2019pim we include TESS points obtained at $\Delta t < 0.1$ day. Our searches tend to find afterglows that are brighter than the bulk of the follow-up sample.

detection 20 minutes later. No associated GRB had been reported. We searched the pointing history of different satellites, and determined that the transient position was visible to Fermi-GBM for 14 minutes out of the 20 minutes in the interval between the last nondetection and the first detection. The position was not visible to Swift-BAT or to SPI-ACS (Vedrenne et al. 2003) onboard the INTernational Gamma-ray Astrophysics Laboratory (INTEGRAL; Winkler et al. 2003): INTEGRAL was not obtaining data due to its regular perigee passage. Konus-Wind was only recording data in its S2 detector, but despite the high incident angle to the source (115 deg), reasonable upper limits on the γ-ray emission may be derived (Section 3.2). We reported the transient to the TNS on January 16.9 and it was assigned the name AT 2021any.

AT 2021any was observed with the Optical Spectrograph and InfraRed Imager System (OSIRIS; Cepa et al. 2000) mounted on the 10.4 m Gran Telescopio Canarias (GTC) telescope at the Roque de los Muchachos Observatory on the island of La Palma (Spain). The observation consisted of 4×900 s exposures with grism R1000B and a $1''$ wide slit, aligned with the parallactic angle (Filippenko 1982), which results in a resolving power of ~ 600 and spectral coverage between 3700 Å and 7800 Å. The observation was performed at a mean epoch of 00:06 UT on 17 January 2021. The data reduction was performed using a custom pipeline based on shell scripts and IRAF routines that included bias, response (flatfielding), wavelength calibration, and flux calibration based on the observation of a spectrophotometric star. Telluric features were not removed.

As mentioned by de Ugarte Postigo et al. (2021a), the spectrum (see Figure 4) shows several prominent absorption features corresponding to Lyα, S II, O I, Si II, Si IV, C II, C IV, Fe II, Al II,

and Al III at a common redshift of $z = 2.5131 \pm 0.0016$. To determine the redshift we use the average value calculated for each of the unblended features, taking their standard deviation as the uncertainty. The equivalent widths measured for these lines are displayed in Table 2, together with their measured wavelength and redshift. The reduced spectra can be plotted and downloaded within the GRBSpec database[42] (de Ugarte Postigo et al. 2014).

Preceding our spectroscopic observations with OSIRIS, we obtained two acquisition images of 60 s and 30 s in the r'-band filter (first reported by de Ugarte Postigo et al. 2021a). The afterglow is clearly detected in each image. No calibration frames were taken for these observations, but the raw images are of high quality.

After a weather-induced delay, we obtained two epochs of observations with the Calar Alto Faint Object Spectrograph (CAFOS) mounted on the 2.2 m telescope of the Centro Astronómico Hispano en Andalucía (CAHA), Almeria, Spain, in the R_C filter (first reported by Kann et al. 2021a and Kann et al. 2021b). The observations consisted of 10×360 s at ~ 1.7 days after the GRB, and another 12×360 s a night later. Observing conditions were fair, but with mediocre seeing. The afterglow is clearly detected in each stack. Images were bias-subtracted, flatfielded, aligned, and stacked with standard procedures in ESO MIDAS[43] and PyRAF[44]. The CAFOS and OSIRIS photometry is presented in Table 6. Additional optical follow-up observations of AT 2021any were reported by a variety of facilities (Kumar et al. 2021; Ahumada et al. 2021; Zhu et al. 2021;

---

[42] http://grbspec.eu
[43] https://www.eso.org/sci/software/esomidas/
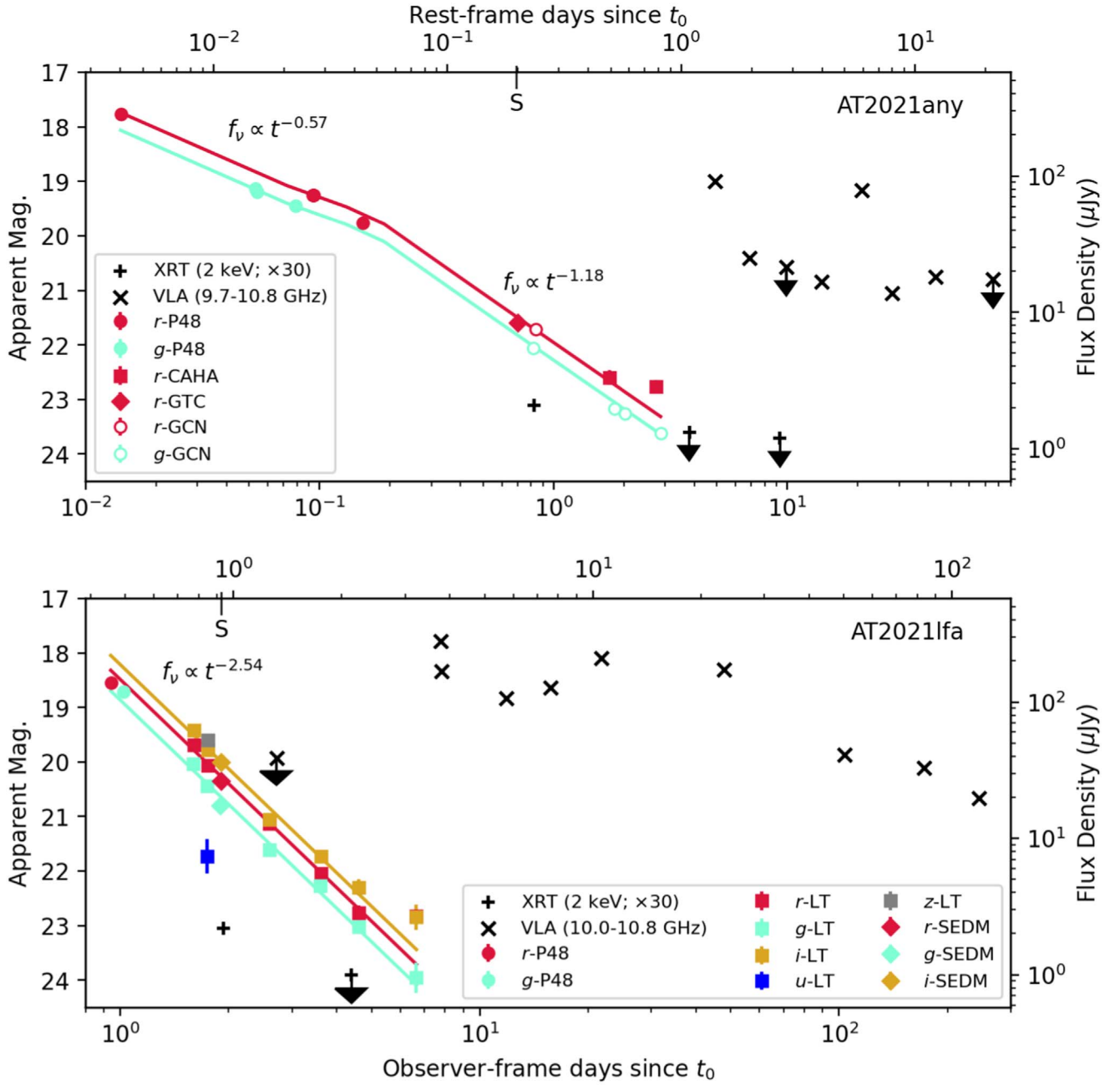[44] https://iraf-community.github.io/pyraf.html

Figure 3. The optical, X-ray, and radio light curves of two new orphan afterglows, AT 2021any (top panel) and AT 2021lfa (bottom panel), together with their best-fit power laws. Data presented in this paper are shown as filled points, with different symbols for different instruments. Data obtained from GCNs (Zhu et al. 2021; Guelbenzu et al. 2021) are shown as unfilled circles. The optical data have been corrected for Milky Way extinction. X-ray data are shown with a plus sign and scaled by a factor of 30 for clarity. Radio X-band data are shown with crosses. Arrows indicate upper limits. An "S" along the top marks an epoch of spectroscopy. The best-fit t_0 is calculated as described in Section 3.2—we caution that these values are uncertain.

Hu et al. 2021; Coughlin & Ahumada 2021; Rossi et al. 2021c; Guelbenzu et al. 2021; Ghosh et al. 2021).

We obtained a Swift-XRT[45] observation of AT 2021any beginning 0.81 days after the first optical detection. We obtained three epochs of 3 ks exposures and reduced the data using the online tool[46] developed by the Swift team (Evans et al. 2007). In the first epoch X-ray emission was detected at the transient position, and there was no detection in the subsequent two epochs. The observation log is provided in

Table 7. Taking a neutral hydrogen column density of $n_{\rm H} = 8.12 \times 10^{20}\,{\rm cm}^{-2}$ (Willingale et al. 2013) and assuming a power-law spectrum with a photon index of $\Gamma = 2$, we find an unabsorbed flux density of $3.30 \times 10^{-13}\,{\rm erg\,cm}^{-2}\,{\rm s}^{-1}$ using webpimms.[47] The X-ray light curve is shown in Figure 3.

We obtained eight epochs of VLA observations of AT 2021any under our ToO program[48]: six epochs were in X band (10 GHz), one epoch was in X and Ku band (15 GHz), and one epoch was in S (3 GHz), C (6 GHz), X, and Ku band.
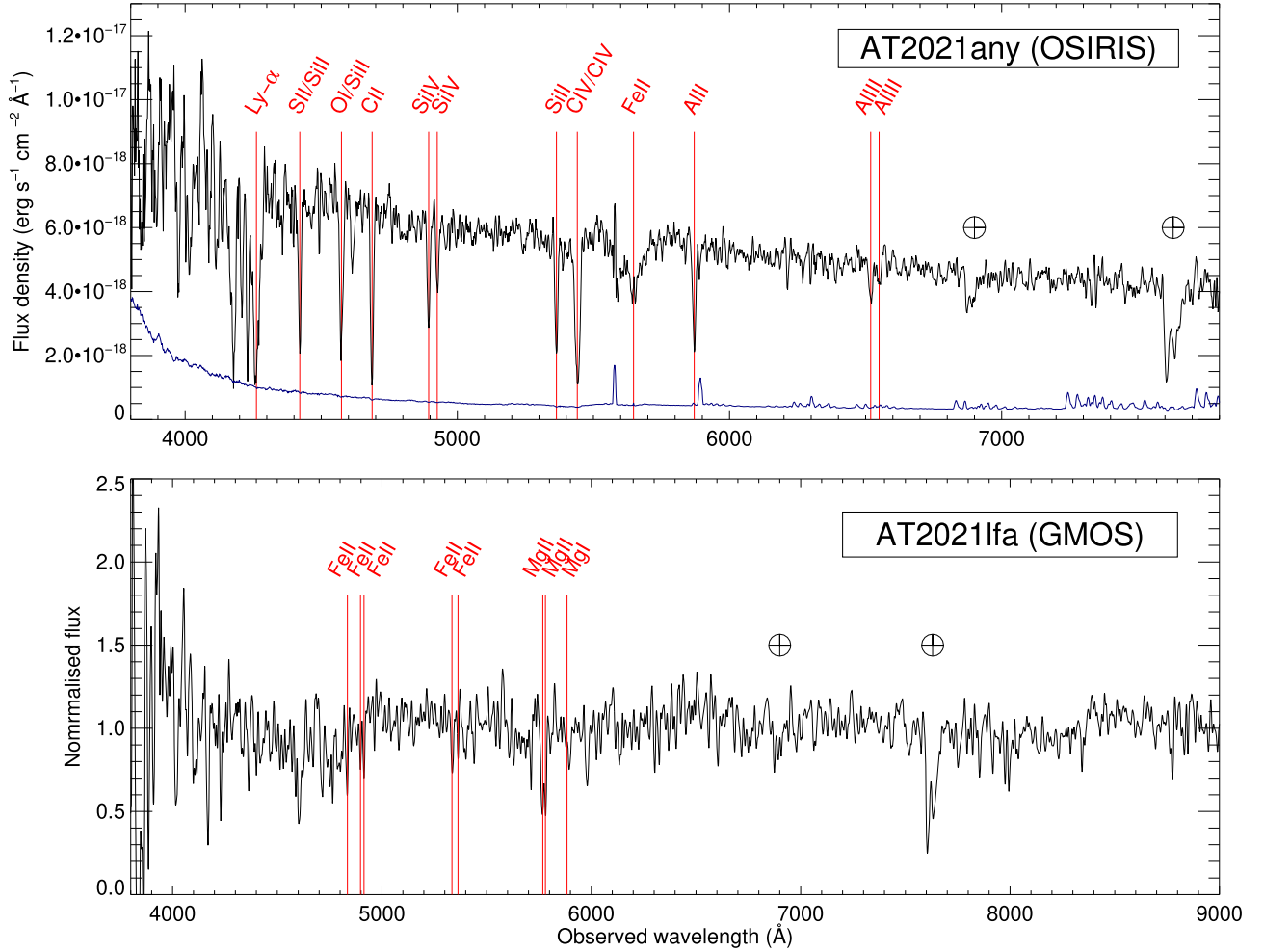

Figure 4. Optical spectra of AT 2021any (top panel; OSIRIS/GTC) and AT 2021lfa (bottom panel; GMOS-S/Gemini), two afterglows with no associated detected GRB. Vertical lines mark absorption features used to measure the redshifts of $z = 2.5131$ (AT 2021any) and $z = 1.0624$ (AT 2021lfa). Regions affected by telluric absorption are also marked. The blue line in the AT 2021any panel is the error spectrum.

Table 2
Equivalent Widths from the Optical Spectra

Name	Obs. λ (Å)	Feature	z	EW (Å)
AT 2021any	4421.02	S II 1259.52	2.5131	7.41 ± 1.26
		Si II 1260.42	2.5131	
	4574.15	O I 1302.17	2.5131	9.31 ± 1.03
		Si II 1304.37	2.5131	
	4686.88	C II 1334.53	2.5120	10.13 ± 0.94
	4894.81	Si IV 1393.76	2.5119	5.38 ± 0.88
	4926.22	Si IV 1402.77	2.5118	3.46 ± 0.77
	5364.17	Si II 1526.71	2.5135	7.81 ± 0.74
	5440.73	C IV 1548.2	2.514	17.58 ± 0.98
		C IV 1550.77	2.5131	
	5647.44	Fe II 1608.45	2.5111	8.98 ± 0.91
	5870.30	Al II 1670.79	2.5135	7.82 ± 0.85
	6518.77	Al III 1854.72	2.5147	2.97 ± 0.64
	6549.65	Al III 1862.79	2.5160	1.49 ± 0.52
AT 2021lfa	4834.99	FeII 2344.21	1.0625	2.51 ± 0.82
	4897.54	Fe II 2374.46	1.0626	2.65 ± 0.85
	4914.12	Fe II 2382.77	1.0624	3.52 ± 0.90
	5334.21	Fe II 2586.65	1.0622	3.12 ± 0.95
	5363.12	Fe II 2600.17	1.0626	3.94 ± 0.92
	5768.26	Mg II 2796.30	1.0628	3.30 ± 0.85
	5780.84	Mg II 2803.50	1.0620	4.63 ± 0.88

The source J0808-0751 was used as a phase calibrator. For most observations 3C138 was used as the flux calibrator, although to account for the recent flaring behavior of this source we also observed 3C286 during the third epoch, and in the final two epochs we observed 3C286 only. Reduction of the data was performed using the Astronomical Image Processing System (AIPS) using standard synthesis imaging techniques. Calibration was performed by hand, and regions of the spectrum heavily contaminated by radio-frequency interference (RFI) were excluded. We publicly reported the first detection (Perley et al. 2021c) and the observations are listed in Table 8. The 10 GHz radio light curve is shown in Figure 3, and the evolution of the radio spectral energy distribution (SED) is shown in Figure 5.

We obtained a deep image of the position of AT 2021any using the Low Resolution Imaging Spectrometer (LRIS; Oke et al. 1995) on the Keck I 10 m telescope. We imaged in four filters (U, G, R, and RG850) with exposure times of 20 minutes per filter. Data reduction was performed using LPipe (Perley 2019). The U, G, and RG850 filters were calibrated relative to the SDSS u, g, and z bands and reported in the AB system. Cousins R-band magnitudes for secondary standards were calculated via the Lupton transform and the magnitudes are reported in the AB system. A faint ($g = 25$ mag) source was detected at the transient position, and the photometry is
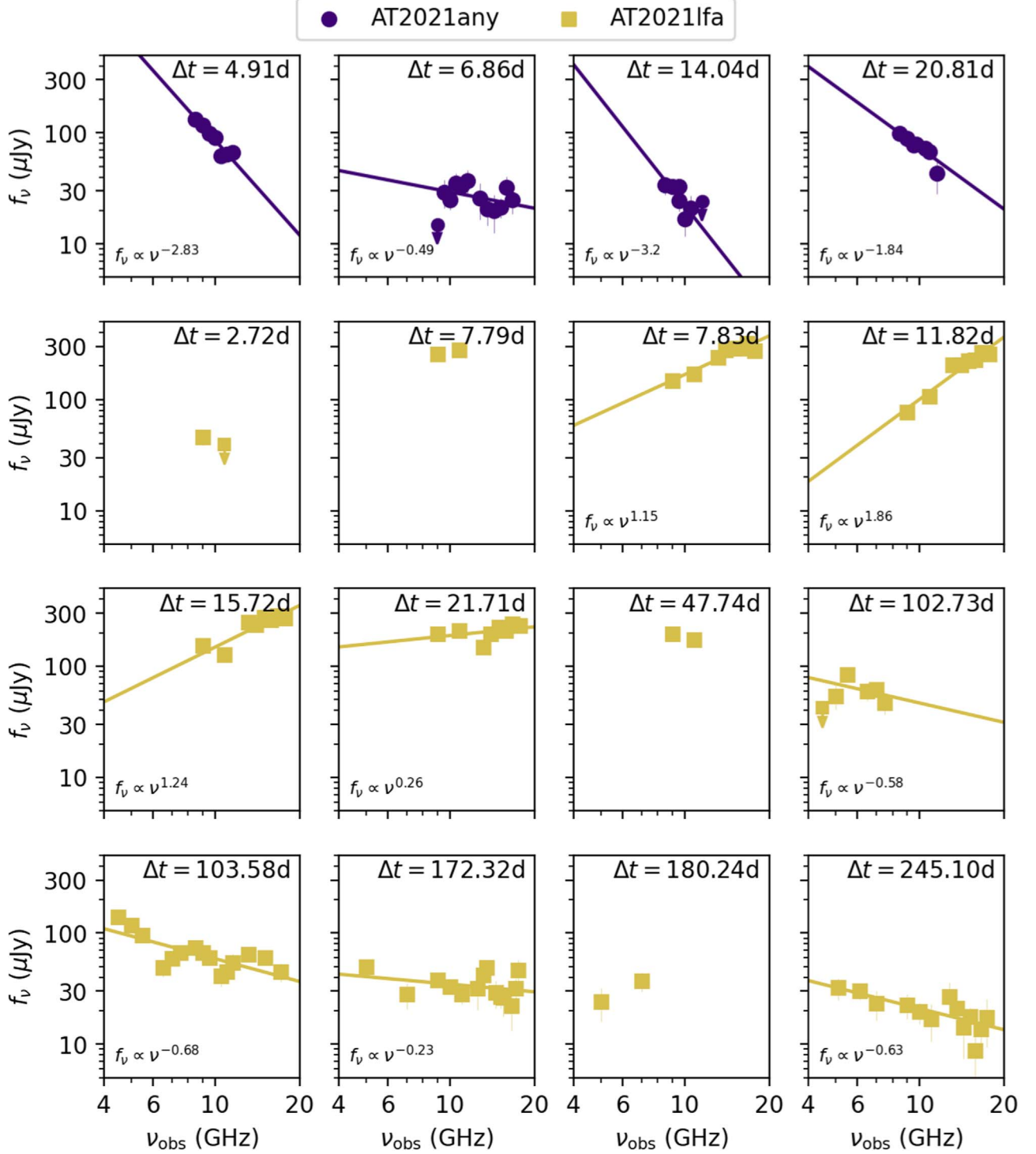
Figure 5. Evolution of the radio SED of AT 2021any (circles) and AT 2021lfa (squares), afterglows with no associated detected GRB. The lines show power-law fits to the data for each epoch with >2 data points. The SEDs of AT 2021any appear optically thin throughout. The SEDs of AT 2021lfa appear self-absorbed up to 21.71 days and then become optically thin, suggesting that the self-absorption frequency has passed through the VLA observing bands. Note that the light curve of AT 2021lfa shows evidence for scintillation at $\nu \lesssim 10$ GHz.

presented in Table 3. The host colors resemble those of a typical LGRB host galaxy.

2.3.3. ZTF 21aagwbjr/AT 2021buv/GRB 210204A

ZTF 21aagwbjr was first detected in an image obtained on 2021 February 04.30 at $r = 17.11 \pm 0.05$ mag as part of the one-day cadence TESS shadowing survey. The previous

nondetection was 1.87 hr prior at $g > 18.25$ mag. The previous r-band nondetection was 1.05 days prior at $r > 20.35$ mag, giving a rise rate in r band of >3.1 mag day^{-1}. There was only one detection the first night. There were four detections the second night, two in r band and two in g band. Owing to the rapid fade rate of 2.15 ± 0.14 mag day^{-1} in r band, the extinction-corrected red color ($g - r = 0.42 \pm 0.19$ mag), and the presence of a faint ($g = 24.6$ mag and $r = 23.7$ mag)

Table 3
LRIS Imaging of Transient Locations to Search for Host Counterparts

Name	Date (UT)	Exposure (s)	U (mag[a])	G (mag)	R (mag)	RG850 (mag)
AT 2021any	2022 January 31	1380	>25.90	...	...	24.99 ± 0.29
...	...	1080	...	25.02 ± 0.10	25.27 ± 0.17	...
AT 2020blt[b]	2022 January 31	960	...	>26.49	>25.92	...
...	2022 February 27	1920	>26.65	...	...	>25.34
AT 2021lfa	2022 March 03	1080	>25.55	...	...	>24.68
...	...	900	...	>26.50	>26.17	...

Notes.
[a] Magnitudes are reported in the AB system.
[b] For the RG850 observation of AT 2020blt, we created custom sky flats for each exposure using dithered images of the field to correct for variations in the flat-field pattern between the science and calibration frame.

counterpart (putative host galaxy) at the transient position in Legacy Survey pre-imaging, the transient was flagged by the daily scanner on February 05.7. ZTF 21aagwbjr was also flagged by the ZTFReST pipeline, and the ZTF photometry was presented by Andreoni et al. (2021).

A search for an associated GRB identified the long-duration GRB 210204A consistent with the position and time of ZTF 21aagwbjr. GRB 210204A had triggered Fermi-GBM (Fermi GBM Team 2021), the Gamma-Ray Detector (GRD) onboard the Gravitational Wave High-energy Electromagnetic Counterpart All-sky Monitor (GECAM; Zhang et al. 2019; Li et al. 2021), Konus-Wind (Frederiks et al. 2021a; Frederiks & Konus-Wind Team 2021), and AstroSat (Waratkar et al. 2021). The trigger time of February 04.27 was 43 minutes prior to the first ZTF detection. IPN localized the burst to a region of $6.7 \deg^2$ (Hurley et al. 2021). The number of expected GRBs detected by IPN in this region over the 1.87 hr window is 2×10^{-5}, so the association is quite secure. The transient was reported (Kool et al. 2021) and saved to the TNS, where it was assigned the name AT 2021buv. The multiwavelength properties of AT 2021buv will be published in a separate paper by H. Kumar et al. (in preparation). Here we summarize the follow-up observations that were obtained.

We measured the redshift of AT 2021buv using a long-slit spectrum obtained with GMOS-S[49] (Gimeno et al. 2016). The observation was conducted in the Nod-and-Shuffle mode with a $1''0$-wide slit, beginning 42.8 hr after the Fermi-GBM trigger. We obtained 2×450 s spectroscopic exposures with the B600 grating and 2×450 s exposures with the R400 grating, providing coverage over the range 3620–9600 Å. We reduced the spectrum using the IRAF package for GMOS, and clearly detected Mg II and Mg I in absorption at $z = 0.876$. The redshift of 0.876 was independently measured using VLT/X-shooter (Xu et al. 2021) from absorption features including fine-structure lines of Fe II, and emission lines of O II, O III, Hβ, and Hα. The GMOS spectrum will be published by H. Kumar et al. (in preparation).

AT 2021buv was also detected in the X-ray (Evans & Swift Team 2021; Kennea et al. 2021) and radio (Chandra et al. 2021) bands. Additional optical photometry has been made available (Teja et al. 2021; Belkin et al. 2021; Rossi et al. 2021a; Gupta et al. 2021) and includes reports of a jet break (Gupta et al. 2021; Rossi et al. 2021a).

2.3.4. ZTF 21aakruew/AT 2021cwd/GRB 210212B

ZTF 21aakruew was first detected in a ZTF image obtained on 2021 February 12.37 at $g = 19.57 \pm 0.21$ mag, as part of the public survey. The last nondetection was 2.0 days prior at $g > 20.88$ mag, giving a rise rate of >0.7 mag day^{-1}. The extinction-corrected color was $g - r = 0.02 \pm 0.26$ mag and there was no host galaxy visible at the transient position in Legacy Survey pre-imaging (down to $g \approx r \approx 24$ mag). Owing to the fast rise and lack of detected host, the transient was noted by the daily scanner on February 12.7.

The uncertainty in the $g - r$ color was not sufficient to determine whether it was as red as expected for optically thin synchrotron emission ($g - r = 0.24$ mag) or as blue as expected for thermal flares ($g - r = -0.17$ mag). To determine the color more precisely, we obtained LT $griz$ imaging on February 12.98. The LT imaging revealed rapid fading of 2.4 mag day^{-1} in the r band and red colors (extinction-corrected $g - r = 0.75 \pm 0.21$ mag). We report our optical photometry in Table 6.

We could not identify any GRB consistent with the position and time of ZTF 21aakruew. We publicly announced the transient (Perley et al. 2021a) and saved it to the TNS, where it was assigned the name AT 2021cwd. After our announcement, the IPN announced that AT 2021cwd was in the localization region of long-duration GRB 210212B detected by Konus-Wind, INTEGRAL, and Swift-BAT (Svinkin et al. 2021a, 2021b). The burst time was 6.2 hr prior to the first ZTF detection. Follow-up optical photometry was obtained by us with LT as well as by other groups (Pozanenko et al. 2021; Nicuesa Guelbenzu & Klose 2021). A conservative estimate of the 3σ IPN localization area is 1286 deg^2 (the BAT coded region cannot be confidently excluded). The number of GRBs expected to be detected by the IPN in this area during the 2 day window is 0.09, so the association is fairly secure. Unfortunately no redshift measurement was obtained of this event.

2.3.5. ZTF 21aayokph/AT 2021lfa

ZTF 21aayokph was first detected in a public ZTF image on 2021 May 04.23 at $r = 18.60 \pm 0.08$ mag. The last nondetection was 1.92 days prior at $r > 20.23$ mag (also in a public-survey image), giving a rise rate in r band of >0.8 mag day^{-1}. The source was detected in both r band and g band the first night, with an extinction-corrected red color of $g - r = 0.17 \pm 0.14$ mag. The nearest object in Legacy Survey pre-imaging was $2''9$ away, at $g=24.2$ mag and $r=23.5$ mag. Owing to the fast rise, red color, and lack of detected host

---

[49] ToO program GS-2021A-Q-124; PI A. Ho

galaxy at the transient position, the transient was flagged by the daily scanner on May 04.7. We searched for an associated GRB; none was identified in the 1.92 day window consistent with the optical transient position. We publicly reported the source (Yao et al. 2021b) and saved it to the TNS, where it was assigned the name AT 2021lfa.

We obtained a long-slit spectrum of AT 2021lfa with GMOS-S[50] starting on 2021 May 05.18, or $\Delta t = 0.95$ days after the first optical detection. The observation was performed in the Nod-and-Shuffle mode with a 1″0-wide slit. We obtained 2×450 s exposures with each of the B600 and R400 gratings, providing coverage over the range 3620–9540 Å. No flux calibration was performed. The spectrum was reduced using the IRAF package for GMOS. We clearly identified absorption lines of Mg II $\lambda\lambda 2796$, 2803 at $z = 1.0624$ in the B600 and R400 spectra. Absorption lines from Mg I and Fe II were marginally detected in the spectra at a consistent redshift. Using the same approach that we used to measure the redshift of AT 2021any, we find $z = 1.0624 \pm 0.0003$. In practice this is a lower limit, and the lack of observed damped Lyα places an upper limit of $z < 2.3$. We publicly reported the redshift measurement (Yao et al. 2021b). The spectrum with our line identifications is shown in Figure 4, and the measured line strengths are reported in Table 2.

We observed the position of AT 2021lfa with Swift-XRT[51] beginning on May 05.23, $\Delta t = 1$ day after the first optical detection (Ho et al. 2021a). We obtained two epochs of 5 ks exposures separated by 2.5 days and reduced the data using the online tool developed by the Swift team. In the first epoch X-ray emission was detected at the transient position with a count rate of $(9.3 \pm 0.17) \times 10^{-3}$ s^{-1}, and there was no detection in the second epoch with a 3σ upper limit of $<4.4 \times 10^{-3}$ s^{-1}. The observation log is provided in Table 7. Taking a neutral hydrogen column density of $n_H = 2.16 \times 10^{20}$ cm^{-2} and assuming a power-law spectrum with a photon index of $\Gamma = 2$, `webpimms` gives an unabsorbed 0.3–10 keV flux density of 3.5×10^{-13} erg cm^{-2} s^{-1}. The X-ray measurements are shown in Figure 3.

We obtained follow-up observations with the SEDM and LT, which showed rapid fading of 1.9 mag day^{-1} in the r band. LT image reduction was provided by the basic IO:O pipeline. P60 and LT image subtraction was performed following Fremling et al. (2016) using PS1 images for $griz$ and SDSS for u. Our photometric observations are provided in Table 5. Optical photometry was also obtained by other groups (Watson et al. 2021; Butler et al. 2021; Kim et al. 2021; Fu et al. 2021; O'Connor et al. 2021; Pankov et al. 2021a; Rossi et al. 2021b), including a claimed detection 3 hr prior to the first ZTF detection (Lipunov et al. 2021). The r-band light curve is shown in Figure 2, the multiband optical light curve is shown in Figure 3, and the optical SED obtained with LT at $\Delta t = 1.7$ days is shown in Figure 6.

We obtained nine separate epochs of observations of AT 2021lfa with the VLA under our ToO program[52]. The epochs generally involved various combinations of the X, Ku, and C bands, although in one epoch L band was also included, and in some cases an observation was repeated in the lowest-frequency band after a few hours or days to look for evidence of short-timescale scintillation. The observation log is provided
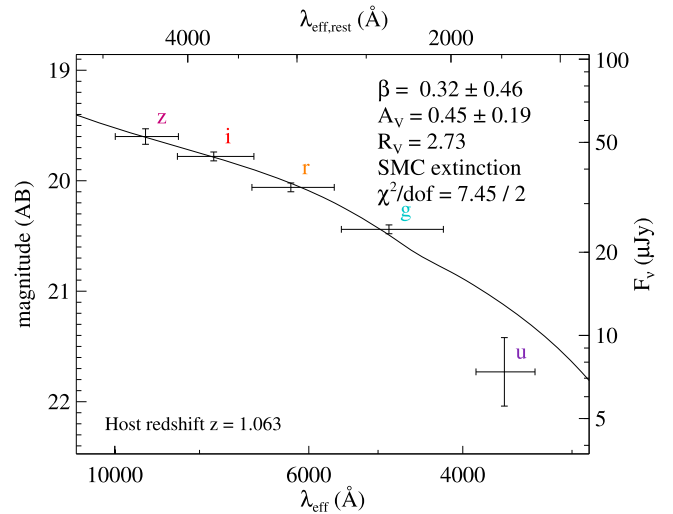
Figure 6. The UVOIR SED of AT 2021lfa, an afterglow with no associated detected GRB. The SED was obtained at $\Delta t = 1.7$ days by LT in the $ugriz$ bands and shows a dropoff before the u band, likely due to extinction. We show a fit to an SMC dust extinction law.

in Table 8. We employed 3C286 as a flux calibrator for all observations and J1224+0330 as the phase calibrator. In three of these epochs we also observed J1407+2827 in the X band only as a polarization leakage calibrator, although no evidence of polarization in the afterglow was detected. Observations were reduced using `AIPS` in the same manner as for the observations of AT 2021any. The 10 GHz radio light curve is shown in Figure 3, and the evolution of the SED is shown in Figure 5.

We obtained a deep image of the position of AT 2021lfa using Keck I/LRIS; the photometry is reported in Table 3. No host counterpart was detected.

2.3.6. ZTF 21abfmpwn/AT 2021qbd/GRB 210610B

ZTF 21abfmpwn was first detected in an image obtained as part of the HC partnership survey on 2021 June 11.23 at $g = 18.49 \pm 0.10$ mag. The last nondetection was 0.85 days prior at $r > 20.20$ mag (in a public survey image), and the most recent nondetection in the same filter was 0.94 days prior at $g > 20.46$ mag (also in a public survey image). The rise time was therefore >2.1 mag day^{-1} in the g band. The daily scanner promptly identified ZTF 21abfmpwn as the afterglow to the Swift LGRB 210610B (Page et al. 2021), which was known to have a bright associated X-ray and optical afterglow at $z = 1.1345$ (Fynbo et al. 2021; de Ugarte Postigo et al. 2021b; Dutta et al. 2021). GRB 210610B was also detected by Fermi-GBM (Malacaria et al. 2021) and Konus-Wind (Frederiks et al. 2021b). The burst time was 9.7 hr before the first ZTF detection.

The transient would have passed our selection criteria regardless of the known GRB association owing to its rapid rise, its red color (extinction-corrected $g - r = 0.32 \pm 0.07$ mag), significant intranight fading (0.32 mag in 3.1 hr, or 2.5 mag day^{-1}), and faint ($g = 23$, $r = 23$ mag) object 0″3 away in Legacy Survey pre-imaging. We publicly reported the ZTF detection (Perley et al. 2021d) and saved the afterglow to the TNS, where it was assigned the name AT 2021qbd. We provide the ZTF photometry in Table 6.

Because AT 2021qbd was associated with a well-observed GRB, we did not obtain any further follow-up observations.
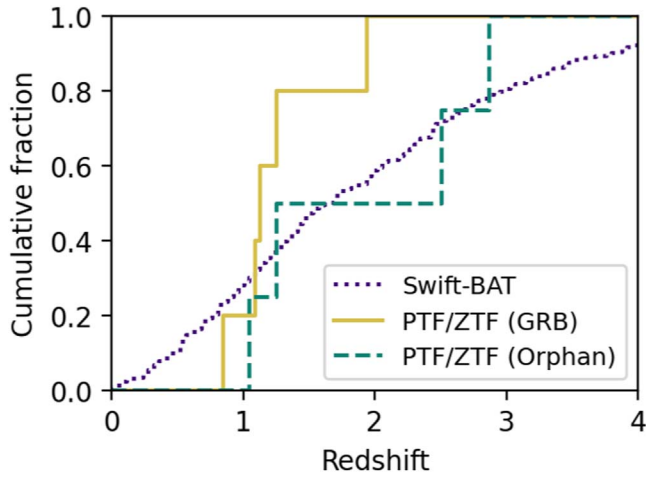
Figure 7. Cumulative redshift distribution of optically discovered afterglows with (five events; solid line) or without (four events; dashed line) associated detected GRBs. For reference we show the distribution for afterglows discovered in follow-up observations to triggers from Swift-BAT (dotted line). The optically discovered events span a wide range of redshifts ($z = 0.9$ to $z = 3$) but the small sample size precludes the discernment of any difference in the populations.

The afterglow was also detected at millimeter (Laskar et al. 2021; Smith et al. 2021) and radio (Alexander et al. 2021) wavelengths.

3. Comparison to the LGRB Population

In this section we compare the properties of the optically discovered afterglows to the population of optical afterglows detected in follow-up observations of GRB triggers.

3.1. Redshift Distribution

In Figure 7 we show the cumulative redshift distribution of all optically discovered events to date compared to that of Swift-BAT GRBs with optical afterglows.[53] Current optical searches sample a wide range of redshifts, from $z = 0.9$ to $z = 3$. However, we cannot discern any statistically significant differences between the optically selected and GRB-selected events at this stage owing to the small sample size. In the future, it will be interesting to see whether the orphan events lie at different redshifts from the events with associated detected GRBs.

3.2. Prompt Emission

To compare the prompt emission properties of the optically discovered afterglows to the GRB-discovered population, we begin by calculating the basic properties of the accompanying GRB for each event, which are summarized in Table 4. For events with probable associated GRBs (as established in Section 2), we calculate the time interval containing 5% to 95% of the burst fluence (T_{90}), the fluence, the isotropic-equivalent γ-ray energy release $E_{\gamma,\mathrm{iso}}$ and luminosity $L_{\gamma,\mathrm{iso}}$, and the peak energy E_p. Because all the bursts were detected by Konus-Wind, we use the same approach as that used by Tsvetkova et al. (2017) and Tsvetkova et al. (2021). For bursts also detected by Fermi-GBM, we confirmed that the energetics inferred from the Fermi-GBM data are consistent with the

Konus-Wind values. We recalculated these values even for previously published events in order to provide consistent measurements.

For orphan events, we estimate the time of an associated burst using a power-law fit to the optical light curve, and use the coverage by high-energy satellites during the relevant period to set limits on the properties of an associated GRB. Because Fermi-GBM and Konus-Wind operate using a flux-based trigger, we use the estimated flux sensitivity to set an upper limit on $L_{\gamma,\mathrm{iso}}$. However, because $E_{\gamma,\mathrm{iso}}$ is an important physical quantity for drawing comparisons with the LGRB population, we also use a typical fluence threshold to estimate an upper limit on $E_{\gamma,\mathrm{iso}}$. The upper limits on $L_{\gamma,\mathrm{iso}}$ and $E_{\gamma,\mathrm{iso}}$ in Table 4 have cosmological corrections applied.

We fit the AT 2021any ZTF light curve with a broken power law following the procedure applied to AT 2020blt (Ho et al. 2020a), which made use of a modified fitting function from Zeh et al. (2006). We fit the function to the g-band and r-band light curves simultaneously, with a constant offset in magnitude between the light curves. Since the host galaxy is not detected in deep Legacy Survey pre-imaging, and the ZTF points are all brighter than 20 mag, we do not fit for a constant offset from the host. Using the `curve_fit` package in `scipy`, we find a best-fit t_0 that is 9 minutes after the last nondetection and 11 minutes prior to the first detection.

The best-fit temporal power-law index is $\alpha_1 = 0.57 \pm 0.04$ prior to the break, and $\alpha_2 = 1.18 \pm 0.01$ after the break, with a break at $\Delta t = 3.9$ hr. The goodness of fit is $\chi^2/\nu = 3.4$ for $\nu = 8$ degrees of freedom. The pre-break index we measure is shallower than the value of $\alpha_1 = 0.89 \pm 0.03$ reported by Gupta et al. (2022) on the basis of GCN photometry. The post-break index we measure is shallower than the value of $\alpha_2 = 2.30$ reported by Kann et al. (2021b). The best fit is shown in Figure 3.

We fit the AT 2021lfa light curve to a single power law, to the g, r, and i light curves simultaneously, with a constant offset in magnitude between each pair of bands. Since the host galaxy is not detected in deep Legacy Survey pre-imaging, we do not fit for a constant offset from the host. We find a best-fit t_0 of May 03.29, which is 0.98 days prior to the first detection and 0.94 days after the last nondetection. The best-fit temporal power-law index is $\alpha = 2.54 \pm 0.02$, with a goodness of fit of $\chi^2/\nu = 4.7$ for $\nu = 18$ degrees of freedom. The fits do not capture an apparent late-time flattening in the r-band and i-band light curves. The fit is shown in Figure 3.

Our best-fit t_0 for AT 2021any is within the interval of visibility of Fermi-GBM. Using the Fermi-GBM trigger sensitivity, we estimate that the upper limit on the peak flux is 1×10^{-7} erg s^{-1} cm^{-2}, although a ground-based analysis could reduce the sensitivity by a factor of 2–3. However, early optical afterglow light curves can have complex behavior (Kann et al. 2010), so our power-law fit may not be appropriate. To be conservative, we report an upper limit based on Konus-Wind. AT 2021any had only nonstandard Konus-Wind data, so we estimate an upper limit on the flux of 10^{-6} erg cm^{-2} s^{-1} (20–10,000 keV; 3.68 s timescale), a factor of a few higher than typical Konus-Wind peak flux upper limits (Ridnaia et al. 2020). For the fluence, a conservative upper limit is 10^{-5} erg cm^{-2} (Tsvetkova et al. 2021). The corresponding limits on the energetics, with cosmological corrections, is $L_{\mathrm{iso}} < 5.0 \times 10^{52}$ erg s^{-1} and $E_{\mathrm{iso}} < 14.3 \times 10^{52}$ erg.

Table 4
Properties of (or Limits on) the Prompt γ-ray Emission Accompanying Afterglows Discovered by Optical Surveys[a]

Name (GRB)	Inst.[b]	T_{90}[c] (s)	Fluence (10^{-6} erg cm^{-2})	Peak Flux (10^{-6} erg cm^{-2} s^{-1})	E_p[c,d] (keV)	$E_{\gamma,\mathrm{iso}}$[e] (10^{52} erg)	$L_{\gamma,\mathrm{iso}}$[e] (10^{52} erg s^{-1})	Ref.[f]
PTF11agg	...	...	<0.4	<0.4	...	...	...	
iPTF14yb (140226A)	IKO	13.5 ± 1.1[g]	$5.1^{+5.6}_{-0.9}$	$0.64^{+0.72}_{-0.14}$	453^{+1010}_{-198}	$5.4^{+6.0}_{-1.0}$	$2.0^{+2.3}_{-0.4}$	
ATLAS17aeu (170105A)	AIKP	3.3 ± 0.6[h]	$2.39^{+0.12}_{-0.15}$	$0.75^{+0.04}_{-0.05}$	56^{+1}_{-12}	...	...	
AT2019pim[i]	...	...	< 0.35	<0.04	...	<0.3	<0.03	[1]
AT2020blt	...	...	<0.4	<0.2	...	<1.0	<1.3	this work; [2]
AT2020kym (200524A)	AFK	66.0 ± 9.9	$34.8^{+4.3}_{-3.9}$	$6.33^{+1.04}_{-0.99}$	215^{+28}_{-27}	$13.6^{+1.7}_{-1.5}$	$5.6^{+0.9}_{-0.9}$	
AT2020sev (200817A)	FIKS	388.6 ± 26.5	$6.6^{+4.3}_{-0.9}$	$0.38^{+0.26}_{-0.07}$	427^{+812}_{-171}	...	...	
AT2020yxz (201103B)	GIK	63.6 ± 20.2[j]	$52.6^{+5.0}_{-4.7}$	$14.9^{+1.4}_{-1.4}$	403^{+44}_{-39}	$16.9^{+1.6}_{-1.5}$	$10.1^{+0.9}_{-0.9}$	
AT2021any	...	...	< 10.0	<1.0	...	<14.3	<5.0	
AT2021buv (210204A)	ABCFIKOS	197.0 ± 6.0	$80.9^{+5.4}_{-6.8}$	$5.6^{+1.06}_{-1.05}$	137^{+13}_{-11}	$22.6^{+1.5}_{-1.9}$	$2.9^{+0.6}_{-0.5}$	
AT2021cwd (210212B)	IK	41.2 ± 2.9[j]	$8.7^{+1.7}_{-1.1}$	$0.67^{+0.48}_{-0.16}$	208^{+84}_{-45}	...	...	
AT2021lfa	...	...	<0.4	<0.4	...	<0.12	<0.26	
AT2021qbd (210610B)	FKS	48.5 ± 4.2	$136.0^{+5.5}_{-5.4}$	$10.7^{+1.11}_{-1.07}$	255^{+8}_{-8}	$47.8^{+1.9}_{-1.9}$	$8.0^{+0.8}_{-0.8}$	

Notes.
[a] Uncertainties are given at 1σ confidence. Values were calculated in the 20 keV–10 MeV range (80–1500 keV for T_{90}) unless otherwise specified.
[b] A: ASTROSAT (CZTI); B: GECAM-B (GRD); C: CALET (GBM); F: Fermi (GBM); G: AGILE (MCAL); I: INTEGRAL (SPI-ACS); K: Konus (Wind); O: Mars-Odyssey (HEND); P: TG2 (POLAR); S: Swift (BAT).
[c] T_{90} and E_p values are presented in the observer frame.
[d] E_p was measured using the time-integrated spectrum.
[e] $E_{\gamma,\mathrm{iso}}$ and $L_{\gamma,\mathrm{iso}}$ have a K-correction applied, which transforms the energetics from the observer-frame 20 keV–10 MeV energy range to the $1/(1 + z)$ keV–10/$(1 + z)$ MeV band.
[f] Quantities were calculated as part of this work unless specified in the Ref. column.
[g] For GRB 140226A, T_{90} was calculated using INTEGRAL (SPI-ACS) data at $\gtrsim$80 keV.
[h] The T_{90} for GRB 170105A is calculated in the 70–300 keV Konus-Wind energy band and is consistent with Stalder et al. (2017). In the softer 20–70 keV band, $T_{90} = 20 \pm 4$ s (more similar to Bhalerao et al. 2017).
[i] The upper limits are measured from a Fermi-GBM targeted search, using a soft template with a 10 s duration.
[j] For GRB 201103B and GRB 210212B, T_{90} is calculated in the 80–1000 keV band.
References. [1] D. Perley et al. (2022, in preparation), [2] Ho et al. (2020a).

For AT 2021lfa, the steep power-law index of the optical light curve suggests that we are observing after the jet break (as discussed in Section 3.4), so we are unable to use our estimated t_0 as a burst time. Given the large window between the last nondetection and the first detection, we use the upper limit on the peak flux from Konus-Wind data of 4×10^{-7} erg cm^{-2} s^{-1} (20–10,000 keV; 2.944 s timescale), giving $L_{\gamma,\mathrm{iso}} < 2.6 \times 10^{51}$ erg s^{-1}. To set an upper limit on the fluence, we searched for a GRB counterpart using the procedure of Tsvetkova et al. (2021). The nondetection suggests that the limiting fluence is comparable to the fluence of the weakest burst from Tsvetkova et al. (2021), so approximately 4×10^{-7} erg cm^{-2} (20 keV–10 MeV). The corresponding upper limits on E_{iso} and L_{iso} are reported in Table 4.

We compute new upper limits for PTF 11agg in a consistent way. The interval of interest is the 21.5 hr between the last nondetection and the first detection. Konus-Wind was taking data with stable background conditions for 98% of the time. We find an upper limit on the peak flux of 4×10^{-7} erg cm^{-2} s^{-1} (20 keV–10 MeV; 2.944 s timescale), which is insensitive to the assumed spectral model. We set a fluence threshold in the same way as for AT 2021lfa.

We can now compare the energetics of the prompt high-energy emission to that of typical LGRBs. The burst durations and L_{iso} values in Table 4 classify each event as a classical LGRB with $L_{\mathrm{iso}} > 10^{49.5}$ erg s^{-1} (Cano et al. 2017). The values of T_{90} range from 3.3 s (for ATLAS17aeu/GRB 170105A) to 388.6 s (for AT 2020sev/GRB 200817A). It is not surprising that we would detect more LGRB

afterglows than short-duration GRB (SGRB) afterglows, because LGRB afterglows are an order of magnitude more luminous than SGRB afterglows (Kann et al. 2011; Berger 2014).

For the orphan events we cannot rule out an associated prompt LGRB with a "classical" high luminosity of $L_{\gamma,\mathrm{iso}} > 10^{49.5}$ erg s^{-1} (Cano et al. 2017). This can be understood as follows. For most events, the coverage by sensitive detectors such as Swift-BAT and Fermi-GBM, together with the uncertainty on the burst time, means that the most robust upper limit comes from Konus-Wind. The Konus-Wind flux threshold of a few $\times 10^{-7}$ erg cm^{-2} s^{-1} could only rule out a $10^{49.5}$ erg s^{-1} GRB at $z = 0.16$ (800 Mpc), a much lower redshift than any of our events.

The cumulative distributions of the prompt energetics are shown in Figure 8. For comparison, we display the distribution of GRBs in the Fermi-GBM Burst Catalog[54] (Gruber et al. 2014; von Kienlin 2014; Narayana Bhat et al. 2016; von Kienlin et al. 2020; Poolakkil et al. 2021), and LGRBs from Konus-Wind with redshift measurements (Tsvetkova et al. 2017). The sample size is too small to discern statistically significant differences. However, so far it appears that if the orphan events are ordinary LGRBs, the bursts have lower luminosities and energies than the events with detected LGRBs. The limits are consistent with a picture in which the GRB-associated events have higher luminosities and energies,
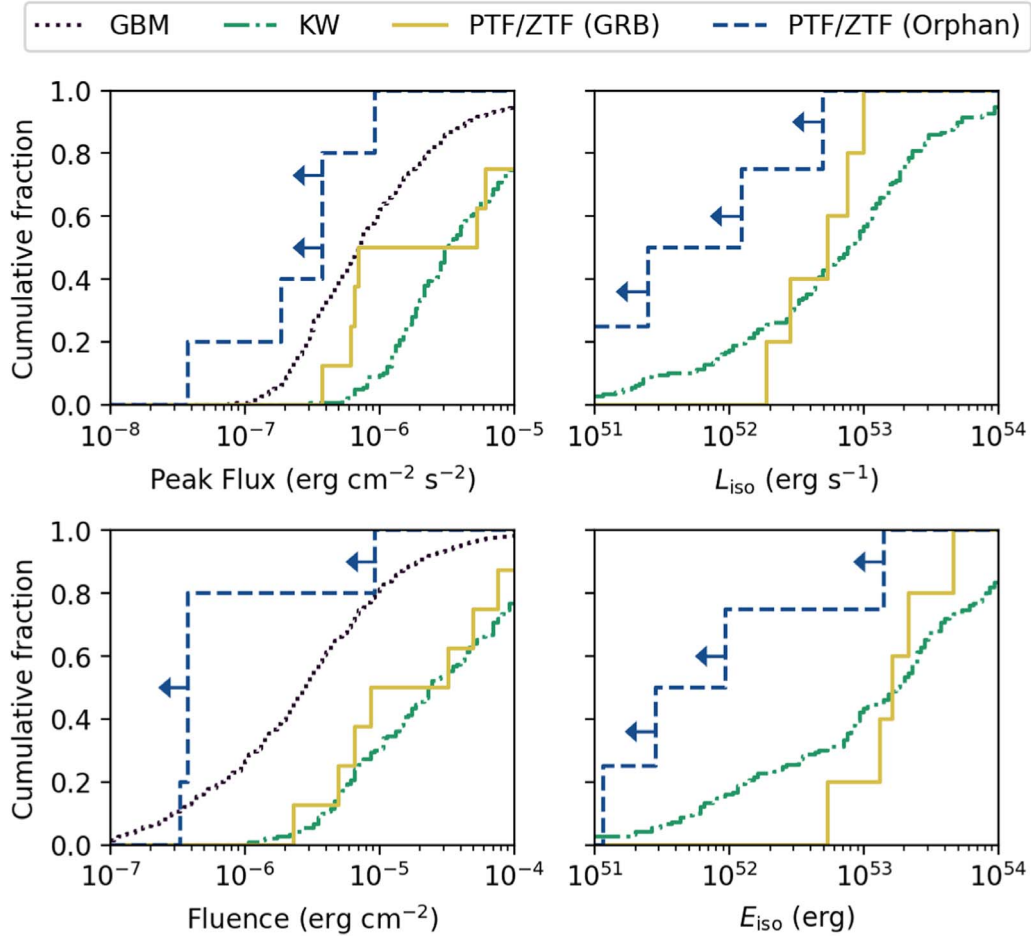
_____

[54] https://heasarc.gsfc.nasa.gov/W3Browse/fermi/fermigbrst.html

Figure 8. Cumulative flux (top left), $L_{\rm iso}$ (top right), fluence (bottom left), and $E_{\rm iso}$ (bottom right) distributions of optically discovered afterglows: events with detected GRBs (solid line) and orphan events (dashed line). For the orphan events, we set the values equal to the upper limit. For comparison, we show the distributions of GRB-selected events from GBM (dotted) and Konus-Wind (dashed–dotted). The sample size is small, but it appears that LGRBs accompanying the orphan events would have to be less luminous and less energetic than the detected LGRB counterparts.

making them detectable by all-sky GRB monitors, whereas the orphan events have lower but still ordinary LGRB parameters.

3.3. Optical Light Curves

In Figure 2 we show the r-band light curves of the ZTF afterglows compared to the sample of optical afterglows detected in follow-up observations of Swift-BAT GRBs presented by Kann et al. (2010), and of Fermi-GBM GRBs presented by Singer et al. (2015). The shaded region indicates the 25th and 75th percentile bounds of the Kann et al. (2010) sample. The left panel shows the events with GRB associations, including two events detected prior to ZTF (iPTF14yb and ATLAS17aeu), and the right panel shows the events with no associated detected GRB, including one event detected prior to ZTF (PTF11agg). The left panel of Figure 2 demonstrates that the events with detected GRBs have particularly bright afterglows—most events are brighter than the 75th percentile from the Kann et al. (2010) sample.

Comparing the brightness of the orphan optical afterglows, shown in the right panel of Figure 2, is challenging because of the uncertainty in the true time of first light. Using the best-fit t_0 values for PTF11agg and AT 2021lfa, the light curves appear to be brighter than those of most GRB afterglows. The best-fit t_0 values for AT 2021any and AT 2020blt suggest that the light

curves are fairly typical in brightness for GRB afterglows. The most extreme case—a value of t_0 equal to the last nondetection —would put the first AT 2020blt detection at $\Delta t = 0.74$ days, and the first AT 2021any detection at $\Delta t = 0.014$ days. So, while AT 2020blt could also have been fairly bright, AT 2021any would still be typical.

For events with measured redshifts, we construct rest-frame u-band optical light curves to compare the optical luminosity of LGRB afterglows. We convert the observed r-band light curves using

$$L_u(t) = 4\pi D_L^2 F_r(t)(1+z)^{-\alpha_{\rm O}+\beta_{\rm O}-1}\left(\frac{\nu_u}{\nu_r}\right)^{-\beta_{\rm O}},\qquad(1)$$

where D_L is the luminosity distance, $F_r(t)$ is the observed r-band flux at a given time t, and z is the redshift. The temporal and spectral indices are defined as $F_\nu \propto t^{-\alpha_{\rm O}}\nu^{-\beta_{\rm O}}$. The frequencies are set to $\nu_u = 8.3 \times 10^{14}$ Hz and $\nu_r = 4.9 \times 10^{14}$ Hz for the u band and r, respectively. For each event we adopt a typical value of $\beta_{\rm O} = 0.6$ (Greiner et al. 2011). The values of $\alpha_{\rm O}$ we adopt for each burst are shown in Table 5, and the resulting light curves are shown in Figure 9. We also take a cross section of the light curves at 11 hr and 1 day in the rest frame; we provide the luminosities in Table 5. The luminosities

Table 5
Properties of the Optical Light Curves for Optically Discovered Afterglows with Redshift Measurements

Name	α_o[a]	L_u[b] (11 hr) (erg s^{-1})	L_u (1 day) (erg s^{-1})	Ref.[c]
iPTF14yb	1.02	8.2×10^{43}	3.4×10^{43}	[1]
AT 2019pim	0.9 (Δt[d] < 3 day), 0 (3 days $< \Delta t < 8$ days), 2 ($\Delta t > 8$ days)	4.4×10^{44}	1.6×10^{44}	[2]
AT 2020blt	0.54 ($\Delta t < 1$ day), 2.62 ($\Delta t > 1$ day)	8.4×10^{44}	1.9×10^{44}	[3]
AT 2020kym	1.53 ($\Delta t < 0.8$ days), 0.8 ($\Delta t > 0.8$ days)	2.5×10^{44}	1.0×10^{44}	
AT 2020yxz	0.96	1.2×10^{45}	4.2×10^{44}	[4]
AT 2021any	0.7 ($\Delta t < 0.8$ days), 2.3 ($\Delta t > 0.8$ days)	4.0×10^{44}	1.9×10^{44}	[5]
AT 2021buv	0.6 ($\Delta t < 2.2$ days), 1.7 ($\Delta t > 2.2$ days)	1.9×10^{45}	4.3×10^{44}	[6]
AT 2021lfa	2.54	2.4×10^{45}	3.9×10^{44}	
AT 2021qbd	1.57	2.0×10^{45}	3.3×10^{44}	[7]

Notes.
[a] Optical temporal power-law decay index.
[b] Rest-frame u-band luminosity.
[c] Reference for the temporal power-law index.
[d] Time ranges are in the observer frame.

References. [1] Cenko et al. (2015), [2] D. Perley et al. in preparation, [3] Ho et al. (2020a), [4] Andreoni et al. (2021), [5] Kann et al. (2021b), [6] Rossi et al. (2021a), and [7] Pankov et al. (2021b).

are typical of LGRB light curves (Racusin et al. 2011) and we find no evidence that the orphan events are distinct.

As a final check, we calculate the rest-frame r-band luminosities of the orphan events at 11 hr, and plot them along with the limits on E_{iso} in Figure 10. We compare them to a sample of LGRBs from Nysewander et al. (2009). For the comparison, we calculate the rest-frame r-band luminosity using the same adopted spectral index ($\beta = 1$) as by Nysewander et al. (2009). The limits on E_{iso} are not sensitive enough to rule out a contemporaneous LGRB for any event.

3.4. Multiwavelength Properties of the Orphan Afterglows

In this section, we analyse the multiwavelength data of AT 2021any and AT 2021lfa, and put the properties of all optical orphan afterglows discovered to date in the context of the LGRB population. Thus far, five orphan optical afterglows have been discovered: PTF11agg ($0.5 \lesssim z \lesssim 3.0$), AT 2019pim ($z = 1.2596$), AT 2020blt ($z = 2.9$), AT 2021any ($z = 2.5131$), and AT 2021lfa ($z = 1.0624$). The properties of PTF11agg and AT 2020blt were presented by Cenko et al. (2013) and Ho et al. (2020a), respectively, and AT 2019pim will be discussed in detail in a separate paper by D. Perley et al. (in preparation). Gupta et al. (2022) analysed the public data of AT 2021any and concluded that its properties were consistent with being a LGRB viewed on-axis. By modeling the optical light curve of AT 2020blt, and adopting deeper limits on the accompanying γ-ray emission than Ho et al. (2020a), Sarin et al. (2022) argued that it was likely viewed on-axis but with an unusually low γ-ray efficiency of $<2.8\%$.

The optical light curves of AT 2021any and AT 2021lfa have temporal indices that are similar to those of LGRB optical afterglows in the literature (Zeh et al. 2006; Kann et al. 2010; Li et al. 2012; Wang et al. 2018). The AT 2021lfa power-law index of $\alpha = 2.54 \pm 0.02$ is close to expectations for synchrotron emission from a power-law distribution of electrons after the edge of the jet is visible, for a typical electron energy power-law index of $p = 2.5$ (Sari et al. 1999). The AT 2021any light curve shows a clear break. The post-break index of $\alpha_2 = 1.2$ is close to expectations for synchrotron
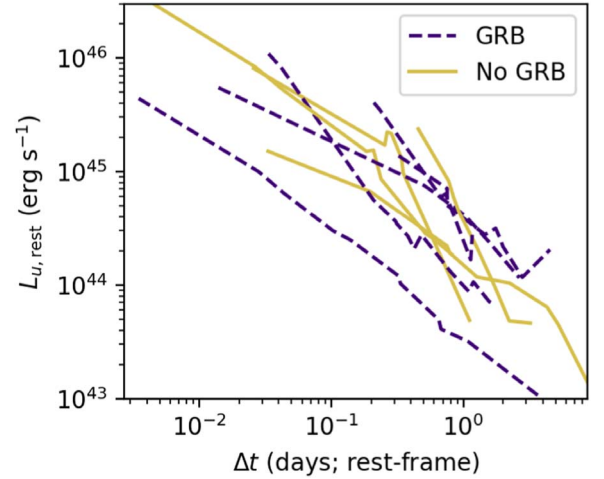

Figure 9. Rest-frame u-band light curves of all optically discovered afterglows with redshift measurements, including events with (dashed line) and without (solid line) associated detected GRBs. There is no clear difference between the GRB-associated and orphan events.

emission before the edge of the jet is visible (Sari et al. 1999). The pre-break index of $\alpha_1 = 0.6$ is quite shallow, and close to the pre-break value measured for AT 2020blt (Ho et al. 2020a).

Light-curve breaks are commonly attributed to two effects in collimated relativistic jets (Rhoads 1997; Sari et al. 1999): sideways expansion and the edge of the jet being visible, both of which are thought to occur when the Lorentz factor is $\Gamma(t) \propto \theta_0^{-1}$, where θ_0 is the opening angle of the jet. The fact that we did not observe the break in AT 2021lfa suggests that it occurred within a day of the burst in the rest frame, which is common for LGRB optical afterglows (Zeh et al. 2006; Kann et al. 2010; Wang et al. 2018), and enables us to estimate the opening angle of the jet. We use the expression from Sari et al. (1999)

$$t_{\mathrm{jet}} = 6.2 \left(\frac{E_{52}}{n_1} \right)^{1/3} \left(\frac{\theta_0}{0.1} \right)^{8/3} \mathrm{hr}, \qquad (2)$$
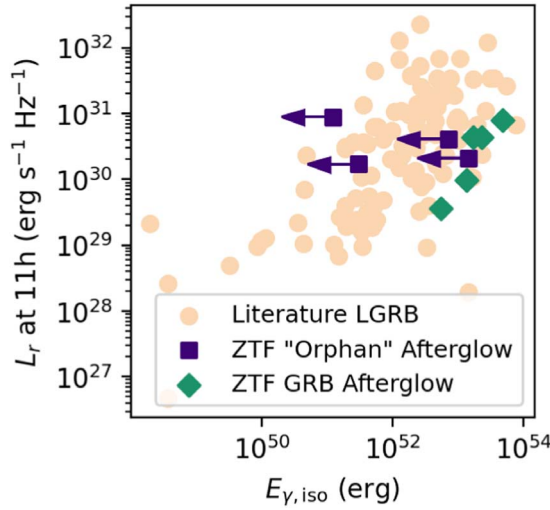
Figure 10. Rest-frame *r*-band luminosities at 11 hr for all optically discovered afterglows with redshift measurements, compared to the LGRB sample from Nysewander et al. (2009). We cannot rule out an associated LGRB for any of the orphan events.

Figure 11. Line-strength diagram comparing the features in the spectra of AT 2021any and AT 2021lfa, two apparently orphan afterglows, with those of a large sample of GRB afterglows. The lines of AT 2021any are stronger than average, but they show similar relative strengths as those of the sample. The line strengths of AT 2021lfa are average for LGRB afterglows.

where E_{52} is $E_{\rm iso}$ in units of 10^{52} erg, n_1 is the circumburst density in units of cm^{-3}, and $t_{\rm jet}$ is the time of the jet break. For AT 2021lfa, we adopt $t_{\rm jet} < 22$ hr and $E_{52} < 0.12$. The opening angle, which is more sensitive to the timing of the break, is therefore $<12°$. For AT 2021any, the shallower decay index suggests that we did not observe the transition. Taking $t_{\rm jet} > 0.6$ days in the rest frame, and $E_{52} < 14.3$, we infer an opening angle of $>6°$.

The optical light curves constrain our viewing angle. For AT 2021any, the shallow ($\alpha = 1.2$) index is consistent with an event viewed directly on-axis, in agreement with Gupta et al. (2022). For AT 2021lfa, from the available photometry we cannot determine whether the event was initially viewed on-axis. However, given the high luminosity, it must have been viewed at least very close to on-axis.

Interestingly, of the five orphan optical afterglows observed so far, all show either a prominent break in the light curve or a steep power-law index consistent with post-break evolution. We discussed AT 2021any and AT 2021lfa above. AT 2020blt had a clear jet break (Ho et al. 2020a). As will be discussed by D. Perley et al. (in preparation), AT 2019pim had a complicated light curve, with several segments having different decay indices: an early segment had $\alpha = 0.9$ while a later segment appeared to show a steeper value of $\alpha = 2$, which could also represent a break. The light curve of PTF11agg was fit by a single power law with index $\alpha = 1.66 \pm 0.35$, but possibly a value as steep as $\alpha = 2.5$ owing to the uncertainty in the burst time. The data are consistent with AT 2021any, AT 2019pim, and AT 2020blt being viewed within the initial opening angle of the jet, while AT 2021lfa and PTF11agg may have been viewed slightly off-axis.

The optical spectra of AT 2021any and AT 2021lfa are also typical of LGRB afterglows. We compare the strength of the redshift-corrected spectral features of each object with those of a large sample of LGRB afterglow spectra. To do this, we calculate a line-strength parameter (LSP; de Ugarte Postigo et al. 2012) and construct a line-strength diagram. The LSP is defined in Equation (1) of de Ugarte Postigo et al. (2012),
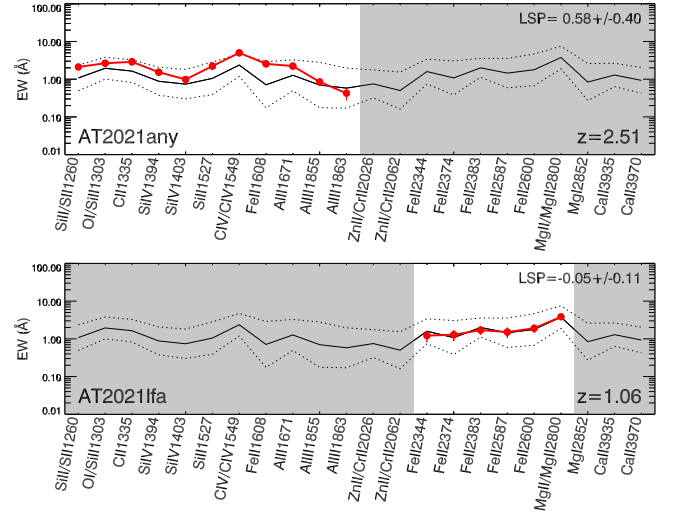
which we reproduce here

$$\mathrm{LSP} = \frac{1}{N}\sum_{i=1}^{N} \frac{\log \mathrm{EW}_i - \langle \log \mathrm{EW}\rangle_i}{\sigma_{\log \mathrm{EW},i}}, \qquad (3)$$

where EW $_i$ is the equivalent widths of the spectral lined. Essentially, the LSP quantifies the difference between the strength of absorption features in a given spectrum to the strength of an average GRB spectrum: a positive and negative value means stronger and weaker lines, respectively. By calculating the LSP and producing a line-strength diagram, we can identify differences between the composition or ionization of an individual object's environment and the values typical of LGRB environments.

In the case of AT 2021any, we obtain an LSP of 0.58 ± 0.40, which implies that the observed features are stronger than those of 80% of the sample. The line-strength diagram for this spectrum (Figure 11) shows no clear deviations of the relative line strength of the lines with those of the sample, except perhaps a slight deficit of Al III. So although the lines are stronger than average, there is no significant difference in the ionization state or composition. For AT 2021lfa we calculate a value of LSP $= -0.05 \pm 0.11$, close to the average of the LGRB sample. The line-strength diagram (Figure 11) also shows a line-strength distribution that follows the average values of the sample, with the same relative strength of lines.

The optical to X-ray SEDs of AT 2021any and AT 2021lfa are also typical of LGRBs. For AT 2021any we take the Nordic Optical Telescope (NOT) photometry from Zhu et al. (2021) at $\Delta t = 0.8$ days, and find a spectral index of $\beta_{\rm O} = 1.00 \pm 0.01$ across the *gri* bands where $f_\nu \propto \nu^{-\beta_{\rm O}}$. At this epoch, the spectral index from the optical to X-ray band is shallower, $\beta_{\rm OX} = 0.6$. We show the ultraviolet–optical–infrared (UVOIR) SED of AT 2021lfa in Figure 6. The best-fit observed spectral index is $\beta_{\rm O} = 1.24 \pm 0.01$, including a rapid drop between the *g* and *u* bands, which implies host dust extinction. By fitting an extinction law similar to that of the SMC (Fitzpatrick 1999; Gordon et al. 2003), we find $\beta_{\rm O} = 0.32 \pm 0.46$ and $A_V = 0.45 \pm 0.19$ mag. At the epoch of the SEDM observation

0.3 days later, the optical to X-ray index is $\beta_{OX} = 0.4$. The values of β_O, β_{OX}, and A_V are all standard for LGRB afterglows (Cenko et al. 2009; Greiner et al. 2011).

The low signal-to-noise ratio of our X-ray observations precludes a detailed analysis of the X-ray data, so we focus on comparing the overall X-ray luminosity to that of LGRB afterglows. For comparison we use the analysis of Swift/XRT data by Margutti et al. (2013). We estimate the rest-frame 0.3–30 keV luminosity of each of our events, converting the count rate to unabsorbed 0.3–30 keV flux using webpimms. We find $L_X = 2 \times 10^{46}$ erg s^{-1} for AT 2021any and $L_X = 3 \times 10^{45}$ erg s^{-1} for AT 2021lfa. These values are within the typical range of LGRB afterglows at these epochs. We can set upper limits of $t^{-1.0}$ and $t^{-0.3}$ on the fade rate for AT 2021any and AT 2021lfa, respectively, which are consistent with the typical $t^{-1.2}$ in the epochs relevant to our observations (Margutti et al. 2013), and also with the fact that our X-ray data were obtained post-break for AT 2021lfa. Since a jet break should be achromatic (Rhoads 1999), the X-ray light curve would be expected to be steep at this stage.

Our VLA radio observations of AT 2021lfa and AT 2021any constitute the first multifrequency radio observations of optical orphan afterglows having redshift measurements. AT 2020blt had only one detection, at 10 GHz (Ho et al. 2020a). PTF11agg had detailed observations with the VLA and CARMA, but no redshift measurement (Cenko et al. 2013). The spectral luminosities of 10^{31} erg s^{-1} Hz^{-1} at $\Delta t \approx 10$ days are typical of LGRBs (Chandra & Frail 2012).

The 10 GHz radio light curves of AT 2021any and AT 2021lfa, which are shown in Figure 3, exhibit evidence for relatively short-timescale variability. Both show rapid fading from the first to second observation, and the light curve of AT 2021any has an abrupt rebrightening at $\Delta t = 20$ days. The early fading in the light curve of AT 2021lfa represents a factor-of-two flux decrease in a few hours. For AT 2021any, the flux drops by a factor of four from 4.91 days to 6.86 days. The rebrightening at $\Delta t = 20$ days represents a factor of 2–3 change in flux over seven days in the observer frame (two days in the rest frame); the fade represents a factor of 5–6 over the same timescale.

Interstellar scintillation can cause short-term variations at these frequencies, and we find that it likely makes a significant contribution to the light curve of AT 2021any. Scintillation results from small-scale inhomogeneities in the interstellar medium (ISM), which change the phase of an incoming wave front. As the Earth moves, the line of sight to a background source changes, so the net effect is an observed change in flux. The effect is greatest for sources observed at a frequency ν_{obs} that is close to the transition frequency ν_0, which separates strong scattering ($\nu_{obs} < \nu_0$) from weak scattering ($\nu_{obs} > \nu_0$). Using the NE2001 model of the interstellar medium (ISM) (Cordes & Lazio 2002), we find that the positions of AT 2021any and AT 2021lfa have a transition frequency of $\nu_0 = 15$ GHz and $\nu_0 = 8$ GHz, respectively. So, the 10 GHz light curve of AT 2021any is very likely affected by scintillation. The 10 GHz light curve of AT 2021lfa may not be: it is possible that the earliest emission represents a truly distinct emission component, such as a reverse shock (Kulkarni et al. 1999; Sari et al. 1999; Harrison et al. 2001; Laskar et al. 2013; Perley et al. 2014; Laskar et al. 2016).

The SED evolution of AT 2021any is shown in Figure 5. The data at all epochs are fainter with increasing frequency,

suggesting that the emission is optically thin at all epochs (i.e., that the synchrotron self-absorption frequency is $\nu_a < 8$ GHz). We fit a power law of the form $f_\nu = f_0 \nu^\beta$ to each epoch, and find significant changes with time. In particular, the spectral index appears to be steeper ($f_\nu \propto \nu^{-2}$) during the brightest parts of the light curve. The spectral index is shallower ($\nu^{-0.5}$) between brightening episodes, which is a more typical spectral index for GRB afterglows at frequencies below the cooling frequency $\nu_a < \nu < \nu_c$ (Granot & Sari 2002). If the brightening is due to scintillation, it may be that the changing spectral index is also due to the frequency-dependent effects of scintillation.

In the full SED evolution of AT 2021lfa (Figure 6), which spans 7.83–103.58 days, we appear to observe the transition from the optically thick to optically thin regimes. During the epoch 7.83–15.72 days, corresponding to the first peak and rise of the light curve, the data appear to be self-absorbed. We measure a power-law index of $\beta = 1.15 \pm 0.01$ at $\Delta t = 7.83$ days and an index of $\beta = 1.86 \pm 0.02$ at $\Delta t = 11.82$ days. By 21.71 days, the index has become significantly more shallow: we measure $\beta = 0.26 \pm 0.01$. During the fading of the light curve, at 47.74 days and 103.58 days, we measure an optically thin spectral index of $\beta = -0.66 \pm 0.21$ and $\beta = -0.68 \pm 0.01$ (respectively), indicating that the self-absorption frequency has passed through the VLA observing bands, and that the cooling frequency lies above the VLA bands at all epochs of observation.

In conclusion, we do not find any clear differences between the multiwavelength properties of the orphan optical afterglows and the population of LGRBs discovered by high-energy satellites, although we defer detailed modeling of the multi-frequency radio light curves to future work. So, at this stage we have no evidence of a population of optical afterglows that are distinct from LGRBs. We address the implications in Section 4.

4. Discussion

In Section 3.2, we concluded that the optically discovered afterglows resemble the population of on-axis LGRBs in terms of their γ-ray to radio properties. Although the events listed in Table 1 were not selected in a fully consistent way, we can still draw valuable conclusions from the ratio of events with associated detected GRBs to those without.

4.1. Comparison to LGRB Rate

First we compare our detected afterglow rate to the LGRB rate. To do this, we adopt an approach similar to that of Cenko et al. (2013): construct a mock catalog of LGRBs, adopt a light curve from the Swift/BAT follow-up sample obtained with the P60 telescope (Cenko et al. 2009), then check how many of these events would have been discovered by us using ZTF by folding the light curve through the log of ZTF observations.

We created a log of all the observations in which we could have reliably discovered an afterglow. To be conservative, we only used field-nights in which an event could have been recognized via intranight fading. We used ztfquery and the ZTF observation log to select all field-nights in the years 2020 and 2021 with the following criteria:

1. A typical limiting magnitude fainter than 20 mag.
2. At least two r-band observations that night.
3. An r-band observation the previous night in the same filter with a limiting magnitude fainter than 20 mag.
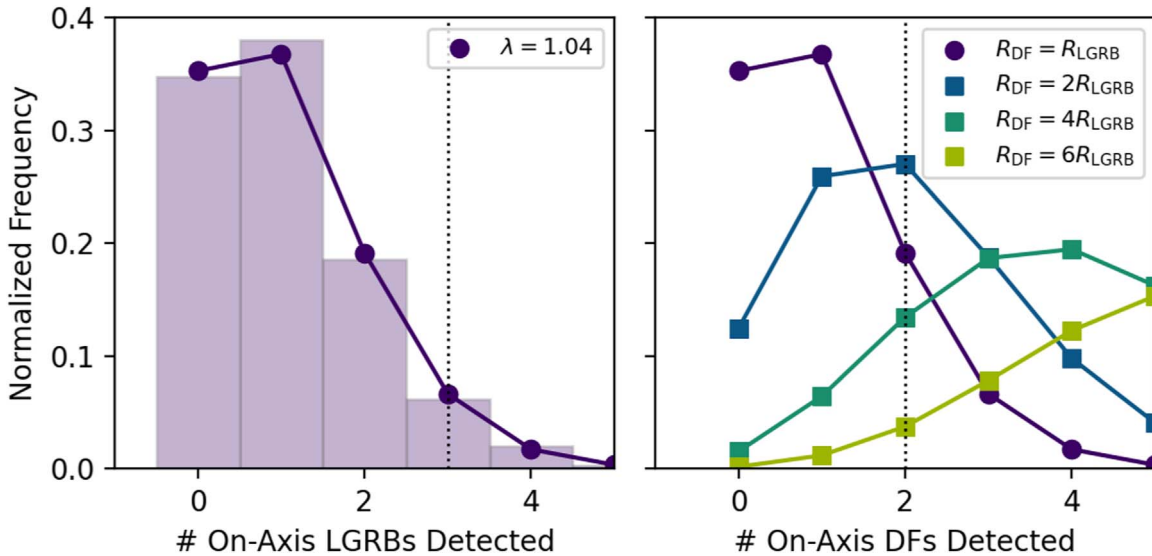4. A field with a Galactic latitude of $|b| > 15°$.

Figure 12. Left): the simulated number of LGRB afterglows serendipitously detected by ZTF as intranight transients in two years of observations (2020 and 2021) based on the all-sky Swift/BAT rate, the sample of Swift/BAT afterglows from Cenko et al. (2009), and 1000 Monte Carlo trials. The distribution is well described by a Poisson function with $\lambda = 1.04$. The vertical dotted line shows the observed number, including one LGRB-associated and two orphan events. (Right): the simulated number of dirty fireballs serendipitously detected by ZTF for four different hypothetical relative rates. The vertical dotted line shows the number of observed orphan afterglows. If both are dirty fireballs, their rate does not exceed $6\times$ the LGRB rate (95% confidence). If neither are dirty fireballs, then the upper limit is $3\times$ the LGRB rate (95% confidence). Note that the true number of ZTF-detected afterglows is higher; we consider a restricted sample for the rate estimate to ensure completeness.

Applying the criteria above resulted in an observation log of 19,190 field-nights and 35,171 unique observations. We used `ztfquery` to estimate a typical limiting magnitude for each of the field-nights in each filter.

Next, we constructed a mock catalog of LGRBs. In the last few years, Swift/BAT detected an average of 73 LGRBs yr^{-1}. Accounting for the field of view and duty cycle in the same way as Cenko et al. (2013), we estimate an all-sky rate of 511 yr^{-1}, slightly less than the rate of 630 yr^{-1} adopted by Cenko et al. (2013) (which included SGRBs). In two years of ZTF, we therefore expect there to be 1022 LGRBs. We assigned each of our 1022 mock GRBs a random burst time t_0, uniformly distributed between 2020 January 1 and 2021 December 31; a random R.A. and Decl. uniformly distributed across the sky; and a random GRB R-band light curve based on the sample of Cenko et al. (2009). We excluded four events—GRB 050607, GRB 060110, GRB 071003, and GRB 071011—because they had Galactic latitudes of $|b| < 15°$. For the light curve, we obtained P60 R_C-band data from Cenko et al. (2009), and in some cases added photometry from the literature (Cenko et al. 2006b; Soderberg et al. 2007; Perley et al. 2008; Covino et al. 2008; Littlejohns et al. 2012). If the data did not extend to below the ZTF detection threshold, we extrapolated the light curve using the best-fit power law from Cenko et al. (2013).

We considered nine bursts "dark" to the P48.[55] For the remainder, we sampled the light curve using the ZTF observation log, to check if it would have been identified by us. We defined a detection as being 0.5 mag brighter than the limiting magnitude. We checked if the set of detections met the following criteria:

1. First detection brighter than 20 mag.
2. Pair of detections within the first night with separation Δt, where 0.02 days $< \Delta t < 0.6$ days.

The above criteria were chosen to be a restrictive subset of our filter, so that we can be more confident in our completeness. Note that observations were grouped by field ID, so we ignore overlap between fields. Taking overlap into account would slightly increase the LGRB discovery rate. Three afterglows passed these criteria in 2020 and 2021 (AT 2020blt, AT 2021any, and AT 2021qbd), of which two (AT 2020blt and AT 2021any) were orphan.[56]

We ran the simulation 1000 times, and the resulting number of expected detected LGRB afterglows is shown in the left panel of Figure 12. The vertical dotted line indicates the number of events we detected with ZTF under these criteria (which are more stringent than our actual criteria). We estimate that the probability of detecting one LGRB afterglow is 60%, while the probability of detecting three LGRB afterglows is only 7%; we can therefore be confident that our searches are reasonably complete. Detecting three events appears unlikely, but we cannot formally rule it out, particularly given the uncertainties in the expected number of LGRBs, which we estimate to be $\sim$10%. Thus, from a rate estimate we do not have definitive evidence of a new class of relativistic explosions.

4.2. The Rate of Dirty Fireballs

We did not detect any confirmed new class of relativistic explosions using our experiment, so can set the most robust upper limit to date on the dirty-fireball rate. A longstanding puzzle in the LGRB field is the "baryon loading problem": that to produce γ-rays efficiently, the baryon loading content must be $M \lesssim 10^{-4} M_\odot$ (Piran 2004). In the baryon-rich environment of a massive-star interior, it may be more natural for jets to become mass-loaded, in which case they could not accelerate material to $\Gamma_{\rm init} \gg 100$ (Huang et al. 2002). It has been argued that dirty fireballs would have an energy similar to that of clean

---

[55] GRB 050412, GRB 050915A, GRB 060510B, GRB 060805A, GRB 060923A, GRB 061222A, GRB 070521, GRB 080320, and GRB 050607.

[56] An additional source, AT 2021kym, passes the criteria if field overlap is taken into account.

fireballs (with the energy in lower-Lorentz factor material; Huang et al. 2002) and would be similarly collimated (Rhoads 2003), in which case the optical afterglows would closely resemble each other (Huang et al. 2002).

Even in the extreme case that all three orphan afterglows (AT 2020blt, AT 2021any, and AT 2021lfa) are dirty fireballs, we can dismiss the possibility that dirty fireballs produce optical afterglows similar to those of LGRBs (as originally conceived) and are an order of magnitude more common than LGRBs. This result is not surprising. Cenko et al. (2015) and Ho et al. (2018) searched PTF data for extragalactic fast transients and recovered only one known GRB afterglow (iPTF14yb), already suggesting that dirty fireballs were not a significant population in the fast optical transient sky. Searches for fast X-ray transients have also resulted in the conclusion that the ratio of dirty ($50 \lesssim \Gamma_0 \lesssim 200$) fireballs to LGRBs ($\Gamma_0 \gg 200$) can be no more than a factor of a few (Grindlay 1999; Dermer et al. 1999; Greiner et al. 2000; Nakar & Piran 2003).

To make this limit quantitative, we use the result from our simulation in Figure 12. The right panel of Figure 12 shows the expected number of detected on-axis dirty fireballs for four different hypothetical rates relative to the LGRB rate, assuming the same afterglow properties for both groups. The vertical dotted line displays the number of orphan afterglows detected (AT 2020blt and AT 2021any). For each relative rate, we integrated the Poisson probability distribution function above $N = 2$ to see when we would expect to see at least two events at 95% confidence. Assuming that both are dirty fireballs (which is unlikely), we rule out a scenario in which dirty fireballs produce similar on-axis optical afterglows to ordinary LGRBs and have a rate that is six times the LGRB rate (95% confidence). Assuming neither is a dirty fireball, which we consider more likely, the limit becomes three times the LGRB rate.

The lack of a large population of dirty fireballs has several possible explanations. One possibility is that mass-loaded jets are less likely to escape the envelope. Another is that the process of jet production and propagation somehow precludes the entrainment of matter. A final possibility is that low-Lorentz-factor jets are successful but produce significantly different optical afterglows; for example, if they have a lower energy per solid angle, the optical afterglow would be fainter. Lei et al. (2013) investigated two different jet-launching mechanisms and found that baryon-rich jets tended to be less luminous. A lower-Lorentz-factor outflow could also exhibit a longer plateau phase owing to the longer deceleration time (Shen & Matzner 2012; Duffell & MacFadyen 2015), resulting in suppressed early afterglow emission. As calculated by Ho et al. (2020a), a dirty fireball with $\Gamma_{\rm init} = 10$ would have a deceleration time of 1.2 days. A typical rest-frame u-band luminosity of LGRB afterglows at 1 day in the rest frame is 10^{44} erg s^{-1} (Racusin et al. 2011), about an order of magnitude fainter than the luminosity at which we are discovering afterglows (Figure 9). So, more sensitive searches may be required to test this scenario.

4.3. The Optical Beaming Factor

Finding optical afterglows without a GRB trigger is also of interest as a way to constrain directly the solid angle of the material producing optical afterglow emission, sometimes referred to as the "optical beaming factor," $f_{b,\rm opt}$. As discussed

by Nakar & Piran (2003), the collimation-corrected GRB energy is typically calculated using the optical beaming factor, with an implicit assumption that $f_{b,\rm opt} \approx f_{b,\gamma}$ (Frail et al. 2001; Panaitescu & Kumar 2001). However, until now there has been no direct test of this assumption.

Our work establishes that $f_{b,\rm opt} \approx f_{b,\gamma}$. By the same argument as in Section 4.2, we find $f_{b,\rm opt} < 6 f_{b,\gamma}$ at 95% confidence, if our orphan events were viewed outside the γ-ray emitting region. If the orphan events were simply LGRBs missed by satellites, then we have $f_{b,\rm opt} < 3 f_{b,\gamma}$. This result is consistent with top-hat jet models (the "spherical approximation"), because in these models, the beaming is expected to be similar for all of the relativistic material.

Nakar & Piran (2003) performed a similar exercise and came to a similar conclusion, using X-ray afterglows. They found that the X-ray beaming factor must be close to the γ-ray beaming factor, concluding that the bulk energies at $\Gamma = 200$ (the γ-ray emitting material) and $\Gamma = 10$ (the X-ray emitting material) are similar and that the homogeneous-jet approximation is reasonable. Our work shows that the energies in the γ-ray, X-ray, and optical-emitting material are all similar.

The result that the beaming factor of the afterglow-emitting material is similar to the beaming factor of the γ-ray emitting material is consistent with jet structures predicted by simulations, and the emission predicted from analytical modeling. In collapsar simulations, the jet develops radial and angular structure from its interaction with the dense stellar material (Zhang et al. 2004; McKinney 2006; Tchekhovskoy et al. 2008; Duffell & MacFadyen 2015; Gottlieb et al. 2021). Most relevant for this work is the angular structure: a narrow ultrarelativistic core with a wide mildly relativistic sheath or cocoon, sometimes referred to as a "two-component jet" (see Granot & Ramirez-Ruiz 2010 for a review). The relative amount of energy in the wide and narrow components depends on a number of factors, but is likely at most comparable for successful jets (Ramirez-Ruiz et al. 2002; Nakar & Piran 2017; De Colle et al. 2018). So, the energy per solid angle from the wider component should be significantly lower than that of the narrow component, leading to fainter afterglow emission, as predicted by Nakar & Piran (2017). We would therefore expect to be biased against afterglow emission from the wide-angle material in our current searches for cosmological ($z \gtrsim 1$) transients.

4.4. The Prevalence of Relativistic Jets in Collapsing Massive Stars

By searching for cosmological relativistic explosions in the ZTF data, we have found no clear new phenomenon that is more common than LGRBs. This result has implications for the fraction of CC SNe that harbor central engines and successful, LGRB-energy relativistic outflows. The observed rate of LGRBs has large uncertainties, as does the beaming fraction; from LGRB rates alone, the intrinsic LGRB rate could be anywhere from 0.01% to 1% of the CC SN rate (see Table 10 of Ho et al. 2020b). Radio searches have discovered one likely off-axis afterglow, and have constrained the rate to be 40–240 Gpc^{-3} yr^{-1}, or 0.06%–0.1% of the CC SN rate (Mooley et al. 2022). Our searches support the idea that energetic relativistic outflows are rare, i.e., that the rate is within a factor of a few of the LGRB rate. However, we cannot set any constraints on the prevalence of weaker, lower-energy jets.

5. Summary and Conclusions

In this paper, we presented the discovery of six cosmological fast optical transients discovered by ZTF without a GRB trigger, as well as deep imaging of a previously published seventh event. Our work doubles the number of optically discovered afterglows (for a total of 13 to date). Extragalactic fast transients powered by optically thin synchrotron emission can be efficiently discovered using HC observations, by requiring rapid evolution (to rule out ordinary extragalactic transients like SNe) and red colors (to rule out the primary contaminant, stellar flares). Using rapid-turnaround optical spectroscopy, X-ray, and radio observations, we measured the redshift of almost all of the events, and showed that they closely resemble on-axis LGRB afterglows. Of the ten afterglows discovered by ZTF to date, six had an associated detected LGRB identified in a post facto search. This result rules out the scenario in which low-Lorentz-factor jets ("dirty" or "failed" fireballs) have an energy per solid angle similar to that of clean fireballs and are an order of magnitude more common than classical GRBs, which is consistent with past searches at X-ray and optical wavelengths. In addition, we set the first direct constraint on the optical beaming factor in LGRBs, finding that it must be comparable to the γ-ray beaming factor.

Our searches were originally motivated by the search for dirty fireballs. The discovery of a population of optical afterglows with a rate greatly exceeding the LGRB rate would have lent strong support for their existence (Cenko et al. 2013). However, it is now clear that it is not so simple. It may be more efficient to search for the prompt X-ray emission expected to accompany a dirty fireball, such as the X-ray flashes found by HETE-2 (Sakamoto et al. 2005). This will become possible in the next few years with facilities such as the Space Variable Object Monitor (SVOM; Wei et al. 2016; Cordier et al. 2015) and Einstein-Probe (Yuan et al. 2018), and perhaps in the next decade with facilities like the Gamow Explorer (White et al. 2021). Millimeter-wavelength observations of the reverse shock could help infer the initial Lorentz factor (e.g., Laskar et al. 2019).

In addition, our current searches are not sensitive to fainter populations, such as highly off-axis afterglows or very dirty fireballs with a long deceleration time. Finding off-axis events is essential for studying the LGRB jet structure, and the lack of a significant population of luminous dirty fireballs simplifies the picture. We will address search strategies for finding slower-evolving relativistic explosions in future studies.

Our work has resulted in the discovery of three orphan events of unknown origin, two of which (AT 2021any and AT 2021lfa) are presented in this paper. Ruling out an associated detected LGRB is not straightforward, and at present requires determining the pointing histories of different high-energy satellites; this work benefited from the coordination enabled by IPN. Based on the coverage and sensitivity of the different spacecraft, the simplest explanation for the orphan events is that they were ordinary LGRBs for which the prompt emission was missed. To determine whether this was truly the case, more sensitive high-energy observations would be required. An all-sky facility with a fluence threshold equal to that of BAT (10^{-8} erg cm^{-2}) could rule out an $E_{\gamma,\mathrm{iso}} = 10^{51}$ erg GRB out to $z = 3$, which includes all of the events in our sample. A burst with 10^{50} erg could be ruled out at $z \lesssim 1.5$.

Although our results suggest that dirty fireballs are not significantly more common than classical GRBs, a significantly larger sample of afterglows would be needed to determine whether a population of dirty fireballs exists at a rate less than or comparable to the GRB rate. With a much higher afterglow discovery rate, manual scanning and triggering will be impractical, as it already is for GRBs themselves. This would motivate an optical version of the Swift facility: autonomous candidate identification and triggering for confirmation. Some of the events in our sample could have been intranight triggers, since there was a nondetection followed by a detection on the same night. With a manageable false-positive rate, deep imaging facilities could confirm a candidate based on fade rate and colors. Spectroscopy to measure the redshift, and X-ray and radio follow-up observations to detect the afterglow at other wavelengths, could then be autonomously performed. Given that the typical time from the close of the ZTF shutter to the release of alerts is 8 minutes (Masci et al. 2019), with higher latencies primarily coming from crowded Galactic fields, it is not unreasonable to strive for afterglow identification, classification, and follow-up observations within 30 minutes of core collapse.

Appendix A
Optical Photometry

In Table 6 we provide optical photometry for the afterglows in our sample.

Table 6
Optical Photometry for Afterglows, Not Corrected for Milky Way Extinction

Name	Date (MJD)	Δt^a (days)	Inst.	Filt.	Mag (AB)
AT2021any	59230.2916	0.0141	P48[b]	r	17.92 ± 0.02
AT2021any	59230.3307	0.0532	P48	g	19.35 ± 0.05
AT2021any	59230.3316	0.0541	P48	g	19.41 ± 0.06
AT2021any	59230.3563	0.0788	P48	g	19.67 ± 0.06
AT2021any	59230.3712	0.0937	P48	r	19.40 ± 0.05

Table 6
(Continued)

Name	Date (MJD)	Δt^a (days)	Inst.	Filt.	Mag (AB)
AT2021any	59230.3717	0.0942	P48	r	19.41 ± 0.05
AT2021any	59230.4303	0.1528	P48	r	19.91 ± 0.11
AT2021any	59230.9772	0.6997	GTC	r	21.74 ± 0.08
AT2021any	59232.0096	1.7321	CAHA	r	22.75 ± 0.13
AT2021any	59233.0184	2.7409	CAHA	r	22.92 ± 0.12
AT2020kym	58993.2863	0.0752	P48	r	17.33 ± 0.01
AT2020kym	58993.2886	0.0775	P48	r	17.38 ± 0.02
AT2020kym	58993.3041	0.0930	P48	r	17.63 ± 0.02
AT2020kym	58993.3065	0.0954	P48	r	17.66 ± 0.02
AT2020kym	58994.2141	1.0029	P48	g	21.60 ± 0.21
AT2020kym	58994.2993	1.0882	P48	r	21.33 ± 0.21
AT2021cwd	59257.3697	0.2600	P48	g	19.57 ± 0.09
AT2021cwd	59257.4158	0.3061	P48	r	19.51 ± 0.07
AT2021cwd	59257.9850	0.8753	LT	g	21.65 ± 0.17
AT2021cwd	59257.9860	0.8763	LT	r	20.88 ± 0.13
AT2021cwd	59257.9871	0.8774	LT	i	20.80 ± 0.13
AT2021cwd	59257.9895	0.8798	LT	z	20.53 ± 0.20
AT2021cwd	59258.9459	1.8362	LT	g	23.32 ± 0.32
AT2021cwd	59258.9509	1.8412	LT	r	22.42 ± 0.21
AT2021cwd	59258.9559	1.8462	LT	i	22.57 ± 0.27
AT2021lfa	59338.2324	0.9393	P48	r	18.60 ± 0.08
AT2021lfa	59338.3126	1.0195	P48	g	18.80 ± 0.11
AT2021lfa	59338.8893	1.5962	LT	g	20.12 ± 0.04
AT2021lfa	59338.8920	1.5988	LT	r	19.75 ± 0.03
AT2021lfa	59338.8946	1.6015	LT	i	19.46 ± 0.04
AT2021lfa	59339.0342	1.7411	LT	u	21.73 ± 0.31
AT2021lfa	59339.0376	1.7445	LT	g	20.52 ± 0.04
AT2021lfa	59339.0403	1.7472	LT	r	20.12 ± 0.04
AT2021lfa	59339.0429	1.7498	LT	i	19.82 ± 0.04
AT2021lfa	59339.0456	1.7525	LT	z	19.63 ± 0.07
AT2021lfa	59339.1898	1.8967	SEDM	g	20.88 ± 0.08
AT2021lfa	59339.1925	1.8994	SEDM	r	20.41 ± 0.07
AT2021lfa	59339.1952	1.9021	SEDM	i	20.05 ± 0.08
AT2021lfa	59339.8817	2.5886	LT	g	21.70 ± 0.06
AT2021lfa	59339.8868	2.5936	LT	r	21.19 ± 0.05
AT2021lfa	59339.8917	2.5986	LT	i	21.09 ± 0.07
AT2021lfa	59340.8923	3.5992	LT	g	22.36 ± 0.08
AT2021lfa	59340.8973	3.6042	LT	r	22.10 ± 0.10
AT2021lfa	59340.9023	3.6092	LT	i	21.77 ± 0.10
AT2021lfa	59341.8829	4.5897	LT	g	23.10 ± 0.14
AT2021lfa	59341.8878	4.5947	LT	r	22.83 ± 0.14
AT2021lfa	59341.8928	4.5997	LT	i	22.34 ± 0.15
AT2021lfa	59343.9336	6.6405	LT	g	24.04 ± 0.28
AT2021lfa	59343.9419	6.6488	LT	r	22.88 ± 0.14
AT2021lfa	59343.9501	6.6570	LT	i	22.89 ± 0.23
AT2021qbd	59376.2325	0.4053	P48	g	18.49 ± 0.02
AT2021qbd	59376.2752	0.4480	P48	r	18.23 ± 0.02
AT2021qbd	59376.3206	0.4935	P48	r	18.37 ± 0.02
AT2021qbd	59376.3601	0.5329	P48	g	18.77 ± 0.03
AT2021qbd	59377.2694	1.4422	P48	r	20.30 ± 0.10
AT2021qbd	59377.3326	1.5055	P48	g	20.75 ± 0.14
AT2021qbd	59377.3336	1.5064	P48	g	20.87 ± 0.12
AT2021qbd	59377.3613	1.5341	P48	g	20.80 ± 0.14
AT2021qbd	59377.3959	1.5687	P48	r	20.24 ± 0.10
AT2021qbd	59378.2548	2.4277	P48	r	21.69 ± 0.33
AT2021qbd	59378.3232	2.4961	P48	r	21.14 ± 0.20

Notes.
[a] Time given relative to t_0 as estimated in the text.
[b] P48 values were measured using forced photometry (Yao et al. 2019).

Appendix B
X-Ray Observations

In Table 7 we provide a log of our X-ray observations of the orphan afterglows AT 2021any and AT 2021lfa.

Table 7
0.3–10 keV X-Ray Observations for Afterglows from Swift/XRT

Name	Date (MJD)	Δt[a] (days)	Exp. (ks)	Count Rate (10^{-3} s^{-1})	Flux[b] (10^{-13} erg s^{-1} cm^{-2})
AT 2021any	59231.10	0.83	3.7	7.20 ± 2.00[c]	3.30 ± 0.90
AT 2021any	59234.08	3.80	2.6	<4.70[d]	<2.10
AT 2021any	59239.58	9.31	2.9	<4.30	<1.90
AT 2021lfa	59339.23	1.94	5.0	9.30 ± 1.70	3.50 ± 0.60
AT 2021lfa	59341.69	4.39	5.1	<4.40	<1.60

Notes.
[a] Time given relative to t_0 as estimated in the text.
[b] The conversion from X-ray count rate to unabsorbed flux uses a hydrogen column density listed in the text, and a photon index of $\Gamma = 2$ for all sources.
[c] Uncertainties are 1σ.
[d] Upper limits are 3σ.

Appendix C
Radio Observations

In Table 8 we provide a log of our VLA radio observations of the orphan afterglows AT 2021any and AT 2021lfa.

Table 8
Log of Our VLA Radio Observations of Two Afterglows with No Associated Detected GRBs[d]

Name	Date (MJD)	Δt[a] (days)	Band	ν (GHz)	$\Delta\nu$ (GHz)	F_ν (μJy)	Configuration
AT2021any	59235.19	4.91	X	9.981	3.58	91 ± 5[b]	A
AT2021any	59235.19	4.91	X	10.98	1.79	63 ± 6	A
AT2021any	59235.19	4.91	X	9.0	1.79	116 ± 8	A
AT2021any	59235.19	4.91	X	11.5	0.896	66 ± 9	A
AT2021any	59235.19	4.91	X	10.49	0.896	62 ± 7	A
AT2021any	59235.19	4.91	X	9.51	0.896	99 ± 8	A
AT2021any	59235.19	4.91	X	8.49	0.896	133 ± 9	A
AT2021any	59237.13	6.86	X	9.981	3.58	25 ± 4	A
AT2021any	59237.13	6.86	X	10.98	1.79	33 ± 6	A
AT2021any	59237.13	6.86	X	9.0	1.79	<15[c]	A
AT2021any	59237.13	6.86	X	11.5	0.896	37 ± 9	A
AT2021any	59237.13	6.86	X	10.49	0.896	35 ± 8	A
AT2021any	59237.13	6.86	X	9.51	0.896	29 ± 8	A
AT2021any	59237.13	6.86	Ku	15.1	5.38	21 ± 4	A
AT2021any	59237.13	6.86	Ku	13.58	2.69	20 ± 6	A
AT2021any	59237.13	6.86	Ku	16.62	2.69	24 ± 6	A
AT2021any	59237.13	6.86	Ku	12.81	1.34	25 ± 9	A
AT2021any	59237.13	6.86	Ku	14.31	1.34	20 ± 7	A
AT2021any	59237.13	6.86	Ku	15.85	1.34	32 ± 8	A
AT2021any	59240.17	9.90	S	3.0	1.1	67 ± 14	A
AT2021any	59240.17	9.90	S	3.3	0.64	38 ± 11	A
AT2021any	59240.17	9.90	S	2.7	0.64	<47	A
AT2021any	59240.17	9.90	C	5.1	1.8	<22	A
AT2021any	59240.17	9.90	C	7.0	2.0	34 ± 7	A
AT2021any	59240.17	9.90	C	6.1	3.8	30 ± 5	A
AT2021any	59240.17	9.90	X	10.0	4.0	<21	A
AT2021any	59240.17	9.90	X	9.0	2.0	<27	A
AT2021any	59240.17	9.90	Ku	15.3	5.0	31 ± 6	A
AT2021any	59240.17	9.90	Ku	15.1	2.0	46 ± 9	A
AT2021any	59244.31	14.04	X	9.5	3.1	24 ± 5	A
AT2021any	59244.31	14.04	X	9.0	2.0	32 ± 4	A
AT2021any	59244.31	14.04	X	10.0	2.0	16 ± 4	A
AT2021any	59244.31	14.04	X	8.5	1.0	34 ± 6	A
AT2021any	59244.31	14.04	X	9.5	1.0	32 ± 6	A
AT2021any	59244.31	14.04	X	10.5	1.0	20 ± 6	A
AT2021any	59244.31	14.04	X	11.5	1.0	<24	A
AT2021any	59251.08	20.81	X	9.7	3.6	78 ± 6	A
AT2021any	59251.08	20.81	X	9.0	2.0	89 ± 6	A
AT2021any	59251.08	20.81	X	10.8	1.6	67 ± 9	A
AT2021any	59251.08	20.81	X	8.5	1.0	98 ± 8	A
AT2021any	59251.08	20.81	X	9.5	1.0	78 ± 7	A
AT2021any	59251.08	20.81	X	10.5	1.0	72 ± 11	A
AT2021any	59251.08	20.81	X	11.5	1.0	43 ± 15	A
AT2021any	59258.25	27.97	X	9.7	3.6	13 ± 4	A
AT2021any	59273.11	42.84	X	9.7	3.6	18 ± 3	A
AT2021any	59306.06	75.78	X	9.0	2.0	<12	D
AT2021any	59306.06	75.78	X	10.8	1.6	<17	D
AT2021lfa	59340.01	2.72	X	9.0	2.0	46 ± 7	D
AT2021lfa	59340.01	2.72	X	10.8	1.6	<39	D
AT2021lfa	59345.08	7.79	X	9.0	2.0	254 ± 14	D
AT2021lfa	59345.08	7.79	X	10.8	1.6	279 ± 17	D
AT2021lfa	59345.12	7.83	Ku	13.1	0.9	238 ± 16	D
AT2021lfa	59345.12	7.83	Ku	14.0	0.9	280 ± 17	D
AT2021lfa	59345.12	7.83	Ku	14.9	0.9	288 ± 16	D
AT2021lfa	59345.12	7.83	Ku	15.8	0.9	287 ± 17	D
AT2021lfa	59345.12	7.83	Ku	16.7	0.9	322 ± 18	D

Table 8
(Continued)

Name	Date (MJD)	Δt[a] (days)	Band	ν (GHz)	$\Delta \nu$ (GHz)	F_ν (μJy)	Configuration
AT2021lfa	59345.12	7.83	Ku	17.7	0.9	276 ± 18	D
AT2021lfa	59345.12	7.83	X	9.0	2.0	147 ± 10	D
AT2021lfa	59345.12	7.83	X	10.8	1.6	168 ± 10	D
AT2021lfa	59349.11	11.82	Ku	13.1	0.9	206 ± 15	D
AT2021lfa	59349.11	11.82	Ku	14.0	0.9	206 ± 15	D
AT2021lfa	59349.11	11.82	Ku	14.9	0.9	223 ± 16	D
AT2021lfa	59349.11	11.82	Ku	15.8	0.9	226 ± 16	D
AT2021lfa	59349.11	11.82	Ku	16.7	0.9	264 ± 18	D
AT2021lfa	59349.11	11.82	Ku	17.7	0.9	257 ± 19	D
AT2021lfa	59349.11	11.82	X	9.0	2.0	77 ± 7	D
AT2021lfa	59349.11	11.82	X	10.8	1.6	107 ± 8	D
AT2021lfa	59353.01	15.72	Ku	13.1	0.9	247 ± 16	D
AT2021lfa	59353.01	15.72	Ku	14.0	0.9	237 ± 15	D
AT2021lfa	59353.01	15.72	Ku	14.9	0.9	277 ± 17	D
AT2021lfa	59353.01	15.72	Ku	15.8	0.9	263 ± 17	D
AT2021lfa	59353.01	15.72	Ku	16.7	0.9	287 ± 18	D
AT2021lfa	59353.01	15.72	Ku	17.7	0.9	271 ± 18	D
AT2021lfa	59353.01	15.72	X	9.0	2.0	155 ± 9	D
AT2021lfa	59353.01	15.72	X	10.8	1.6	127 ± 8	D
AT2021lfa	59359.00	21.71	Ku	13.1	0.9	149 ± 12	D
AT2021lfa	59359.00	21.71	Ku	14.0	0.9	196 ± 13	D
AT2021lfa	59359.00	21.71	Ku	14.9	0.9	224 ± 13	D
AT2021lfa	59359.00	21.71	Ku	15.8	0.9	208 ± 13	D
AT2021lfa	59359.00	21.71	Ku	16.7	0.9	239 ± 14	D
AT2021lfa	59359.00	21.71	Ku	17.7	0.9	234 ± 16	D
AT2021lfa	59359.00	21.71	X	9.0	2.0	194 ± 11	D
AT2021lfa	59359.00	21.71	X	10.8	1.6	209 ± 12	D
AT2021lfa	59385.03	47.74	X	9.0	2.0	194 ± 10	DtoC
AT2021lfa	59385.03	47.74	X	10.8	1.6	172 ± 10	DtoC
AT2021lfa	59440.03	102.73	L	1.43	0.4	<585	C
AT2021lfa	59440.03	102.73	L	1.81	0.4	<276	C
AT2021lfa	59440.03	102.73	C	4.5	1.0	<42	C
AT2021lfa	59440.03	102.73	C	5.5	1.0	84 ± 12	C
AT2021lfa	59440.03	102.73	C	6.5	1.0	60 ± 11	C
AT2021lfa	59440.03	102.73	C	7.5	1.0	47 ± 10	C
AT2021lfa	59440.03	102.73	C	5.0	2.0	54 ± 13	C
AT2021lfa	59440.03	102.73	C	7.0	2.0	62 ± 9	C
AT2021lfa	59440.87	103.58	Ku	13.1	2.0	64 ± 7	C
AT2021lfa	59440.87	103.58	Ku	15.1	2.0	60 ± 6	C
AT2021lfa	59440.87	103.58	Ku	17.1	2.0	45 ± 8	C
AT2021lfa	59440.87	103.58	X	8.5	1.0	74 ± 8	C
AT2021lfa	59440.87	103.58	X	9.5	1.0	60 ± 8	C
AT2021lfa	59440.87	103.58	X	10.5	1.0	41 ± 8	C
AT2021lfa	59440.87	103.58	X	11.5	1.0	54 ± 11	C
AT2021lfa	59440.87	103.58	X	9.0	2.0	67 ± 6	C
AT2021lfa	59440.87	103.58	X	11.0	2.0	45 ± 6	C
AT2021lfa	59440.87	103.58	C	4.5	1.0	140 ± 13	C
AT2021lfa	59440.87	103.58	C	5.5	1.0	95 ± 11	C
AT2021lfa	59440.87	103.58	C	6.5	1.0	49 ± 8	C
AT2021lfa	59440.87	103.58	C	7.5	1.0	67 ± 8	C
AT2021lfa	59440.87	103.58	C	5.0	2.0	118 ± 11	C
AT2021lfa	59440.87	103.58	C	7.0	2.0	59 ± 7	C
AT2021lfa	59509.61	172.32	Ku	12.5	1.0	31 ± 11	B
AT2021lfa	59509.61	172.32	Ku	13.5	1.0	49 ± 7	B
AT2021lfa	59509.61	172.32	Ku	14.5	1.0	29 ± 8	B
AT2021lfa	59509.61	172.32	Ku	15.5	1.0	26 ± 8	B
AT2021lfa	59509.61	172.32	Ku	16.5	1.0	22 ± 8	B
AT2021lfa	59509.61	172.32	Ku	17.5	1.0	46 ± 10	B
AT2021lfa	59509.61	172.32	Ku	13.1	2.0	42 ± 7	B
AT2021lfa	59509.61	172.32	Ku	15.1	2.0	27 ± 5	B
AT2021lfa	59509.61	172.32	Ku	17.1	2.0	32 ± 6	B
AT2021lfa	59509.61	172.32	X	9.0	2.0	38 ± 5	B
AT2021lfa	59509.61	172.32	X	11.0	2.0	28 ± 5	B

Table 8
(Continued)

Name	Date (MJD)	Δt^a (days)	Band	ν (GHz)	$\Delta\nu$ (GHz)	F_ν (μJy)	Configuration
AT2021lfa	59509.61	172.32	X	10.0	4.1	33 ± 4	B
AT2021lfa	59509.61	172.32	C	5.0	2.0	50 ± 8	B
AT2021lfa	59509.61	172.32	C	7.0	2.0	28 ± 7	B
AT2021lfa	59517.54	180.24	C	5.0	2.0	24 ± 8	B
AT2021lfa	59517.54	180.24	C	7.0	2.0	37 ± 7	B
AT2021lfa	59582.39	245.10	Ku	15.1	6.1	17 ± 3	B
AT2021lfa	59582.39	245.10	Ku	13.6	3.1	21 ± 5	B
AT2021lfa	59582.39	245.10	Ku	16.6	3.1	13 ± 5	B
AT2021lfa	59582.39	245.10	Ku	12.8	1.5	27 ± 8	B
AT2021lfa	59582.39	245.10	Ku	14.3	1.5	14 ± 6	B
AT2021lfa	59582.39	245.10	Ku	15.8	1.5	8 ± 7	B
AT2021lfa	59582.39	245.10	Ku	17.4	1.5	17 ± 8	B
AT2021lfa	59582.39	245.10	X	10.0	4.1	19 ± 4	B
AT2021lfa	59582.39	245.10	X	9.0	2.0	22 ± 5	B
AT2021lfa	59582.39	245.10	X	11.0	2.0	16 ± 6	B
AT2021lfa	59582.39	245.10	C	6.1	3.8	30 ± 5	B
AT2021lfa	59582.39	245.10	C	7.0	2.0	23 ± 6	B
AT2021lfa	59582.39	245.10	C	5.1	1.8	32 ± 7	B

Notes.
[a] Time given relative to t_0 as estimated in the text.
[b] Uncertainties in radio measurements are given as the quadrature sum of the image rms and a 5% uncertainty in the flux density owing to the flux calibration.
[c] Radio upper limits are 3× the image rms.
[d] Some measurements are not independent, i.e., the same bandpass is broken into windows and also quoted as the full bandwidth together.

ORCID iDs

Anna Y. Q. Ho ⓘ https://orcid.org/0000-0002-9017-3567
Daniel A. Perley ⓘ https://orcid.org/0000-0001-8472-1996
Yuhan Yao ⓘ https://orcid.org/0000-0001-6747-8509
Dmitry Svinkin ⓘ https://orcid.org/0000-0002-2208-2196
A. de Ugarte Postigo ⓘ https://orcid.org/0000-0001-7717-5085
R. A. Perley ⓘ https://orcid.org/0000-0001-7097-8360
D. Alexander Kann ⓘ https://orcid.org/0000-0003-2902-3583
Eric Burns ⓘ https://orcid.org/0000-0002-2942-3379
Igor Andreoni ⓘ https://orcid.org/0000-0003-3768-7515
Eric C. Bellm ⓘ https://orcid.org/0000-0001-8018-5348
Elisabetta Bissaldi ⓘ https://orcid.org/0000-0001-9935-8106
Joshua S. Bloom ⓘ https://orcid.org/0000-0002-7777-216X
Thomas G. Brink ⓘ https://orcid.org/0000-0001-5955-2502
Richard Dekany ⓘ https://orcid.org/0000-0002-5884-7867
José Feliciano Agüí Fernández ⓘ https://orcid.org/0000-0001-6991-7616
Alexei V. Filippenko ⓘ https://orcid.org/0000-0003-3460-0103
Dmitry Frederiks ⓘ https://orcid.org/0000-0002-1153-6340
Matthew J. Graham ⓘ https://orcid.org/0000-0002-3168-0139
Boyan A. Hristov ⓘ https://orcid.org/0000-0001-9556-7576
Mansi M. Kasliwal ⓘ https://orcid.org/0000-0002-5619-4938
S. R. Kulkarni ⓘ https://orcid.org/0000-0001-5390-8563
Harsh Kumar ⓘ https://orcid.org/0000-0003-0871-4641
Russ R. Laher ⓘ https://orcid.org/0000-0003-2451-5482
Alexandra L. Lysenko ⓘ https://orcid.org/0000-0002-3942-8341
Christian Malacaria ⓘ https://orcid.org/0000-0002-0380-0041
A. A. Miller ⓘ https://orcid.org/0000-0001-9515-478X
S. Poolakkil ⓘ https://orcid.org/0000-0002-6269-0452
Reed Riddle ⓘ https://orcid.org/0000-0002-0387-370X
Anna Ridnaia ⓘ https://orcid.org/0000-0001-9477-5437
Ben Rusholme ⓘ https://orcid.org/0000-0001-7648-4142
Volodymyr Savchenko ⓘ https://orcid.org/0000-0001-6353-0808
Jesper Sollerman ⓘ https://orcid.org/0000-0003-1546-6615
Christina Thöne ⓘ https://orcid.org/0000-0002-7978-7648
Anastasia Tsvetkova ⓘ https://orcid.org/0000-0003-0292-6221
Mikhail Ulanov ⓘ https://orcid.org/0000-0002-0076-5228
Andreas von Kienlin ⓘ https://orcid.org/0000-0002-0221-5916

References

Ahumada, T., Della Costa, J., Cenko, B., & Quimby, R. 2021, GCN, 29309
Alexander, K. D., Laskar, T., Kilpatrick, C., et al. 2021, GCN, 30218
Andreoni, I., Coughlin, M. W., Kool, E. C., et al. 2021, ApJ, 918, 63
Andreoni, I., Kool, E. C., Sagués Carracedo, A., et al. 2020a, ApJ, 904, 155
Andreoni, I., Lu, W., Smith, R. M., et al. 2020b, ApJL, 896, L2
Aptekar, R. L., Frederiks, D. D., Golenetskii, S. V., et al. 1995, SSRv, 71, 265
Astropy Collaboration, Price-Whelan, A. M., Sipőcz, B. M., et al. 2018, AJ, 156, 123
Astropy Collaboration, Robitaille, T. P., Tollerud, E. J., et al. 2013, A&A, 558, A33
Atwood, W. B., Abdo, A. A., Ackermann, M., et al. 2009, ApJ, 697, 1071
Barthelmy, S. D., Barbier, L. M., Cummings, J. R., et al. 2005, SSRv, 120, 143
Belkin, S., Novichonok, A., Pozanenko, A., et al. 2020, GCN, 27820
Belkin, S., Pozanenko, A., Klunko, E., et al. 2021, GCN, 29417
Bellm, E. C. 2016, PASP, 128, 084501
Bellm, E. C., Kulkarni, S. R., Barlow, T., et al. 2019a, PASP, 131, 068003
Bellm, E. C., Kulkarni, S. R., Graham, M. J., et al. 2019b, PASP, 131, 018002
Berger, E. 2014, ARA&A, 52, 43
Berger, E., Leibler, C. N., Chornock, R., et al. 2013, ApJ, 779, 18
Bhalerao, V., Kasliwal, M. M., Bhattacharya, D., et al. 2017, ApJ, 845, 152
Blagorodnova, N., Neill, J. D., Walters, R., et al. 2018, PASP, 130, 035003
Blazek, M., Kann, D. A., de Ugarte Postigo, A., et al. 2020, GCN, 27810
Burrows, D. N., Hill, J. E., Nousek, J. A., et al. 2005, SSRv, 120, 165
Butler, N., Watson, A. M., Kutyrev, A., et al. 2021, GCN, 29941

Butler, N. R., Sakamoto, T., Suzuki, M., et al. 2005, ApJ, 621, 884
Cano, Z., Wang, S.-Q., Dai, Z.-G., & Wu, X.-F. 2017, AdAst, 2017, 8929054
Capalbi, M., Perri, M., D'Elia, V., et al. 2020, GCN, 27811
Cenko, S. B., Fox, D. B., Moon, D.-S., et al. 2006a, PASP, 118, 1396
Cenko, S. B., Frail, D. A., Harrison, F. A., et al. 2011, ApJ, 732, 29
Cenko, S. B., Kasliwal, M., Harrison, F. A., et al. 2006b, ApJ, 652, 490
Cenko, S. B., Kelemen, J., Harrison, F. A., et al. 2009, ApJ, 693, 1484
Cenko, S. B., Kulkarni, S. R., Horesh, A., et al. 2013, ApJ, 769, 130
Cenko, S. B., Urban, A. L., Perley, D. A., et al. 2015, ApJL, 803, L24
Cepa, J., Aguiar, M., Escalera, V. G., et al. 2000, Proc. SPIE, 4008, 623
Chambers, K. C., Magnier, E. A., Metcalfe, N., et al. 2016, arXiv:1612.05560
Chandra, P., Bhalerao, V., Misra, K., & Anupama, G. C. 2021, GCN, 29541
Chandra, P., & Frail, D. A. 2012, ApJ, 746, 156
Cordes, J. M., & Lazio, T. J. W. 2002, arXiv:astro-ph/0207156
Cordier, B., Wei, J., Atteia, J. L., et al. 2015, arXiv:1512.03323
Coughlin, M., & Ahumada, T. 2021, GCN, 29316
Coulter, D. A., Foley, R. J., Kilpatrick, C. D., et al. 2017, Sci, 358, 1556
Covino, S., D'Avanzo, P., Klotz, A., et al. 2008, MNRAS, 388, 347
Cowperthwaite, P. S., Berger, E., Villar, V. A., et al. 2017, ApJL,
    848, L17
Dalal, N., Griest, K., & Pruet, J. 2002, ApJ, 564, 209
De Colle, F., Lu, W., Kumar, P., Ramirez-Ruiz, E., & Smoot, G. 2018,
    MNRAS, 478, 4553
de Ugarte Postigo, A., Blazek, M., Janout, P., et al. 2014, Proc. SPIE, 9152,
    91520B
de Ugarte Postigo, A., Fynbo, J. P. U., Thöne, C. C., et al. 2012, A&A,
    548, A11
de Ugarte Postigo, A., Kann, D. A., Blazek, M., et al. 2020, GCN, 27807
de Ugarte Postigo, A., Kann, D. A., Perley, D. A., et al. 2021a, GCN, 29307
de Ugarte Postigo, A., Thoene, C., Agui Fernandez, J. F., et al. 2021b, GCN,
    30194
Dekany, R., Smith, R. M., Riddle, R., et al. 2020, PASP, 132, 038001
Dermer, C. D., Chiang, J., & Böttcher, M. 1999, ApJ, 513, 656
Dey, A., Schlegel, D. J., Lang, D., et al. 2019, AJ, 157, 168
Drout, M. R., Piro, A. L., Shappee, B. J., et al. 2017, Sci, 358, 1570
Duev, D. A., Mahabal, A., Masci, F. J., et al. 2019, MNRAS, 489, 3582
Duffell, P. C., & MacFadyen, A. I. 2015, ApJ, 806, 205
Dutta, A., Kumar, H., Sahu, D. K., et al. 2021, GCN, 30201
Evans, P. A., Beardmore, A. P., Page, K. L., et al. 2007, A&A, 469, 379
Evans, P. A. & Swift Team 2020, GCN, 27798
Evans, P. A. & Swift Team 2021, GCN, 29412
Fana Dirirsa, F., Axelsson, M., Ohno, M., et al. 2020, GCN, 27797
Fausnaugh, M. M., Vanderspek, R., & Team, T. E. S. S. 2019, GCN, 25982
Fermi GBM Team 2021, GCN, 29390
Filippenko, A. V. 1982, PASP, 94, 715
Fitzpatrick, E. L. 1999, PASP, 111, 63
Frail, D. A., Kulkarni, S. R., Sari, R., et al. 2001, ApJL, 562, L55
Frederiks, D., Golenetskii, S., Lysenko, A., et al. 2021a, GCN, 29415
Frederiks, D., Golenetskii, S., Lysenko, A., et al. 2021b, GCN, 30196
Frederiks, D. & Konus-Wind Team 2021, GCN, 29424
Fremling, C., Miller, A. A., Sharma, Y., et al. 2020, ApJ, 895, 32
Fremling, C., Sollerman, J., Taddia, F., et al. 2016, A&A, 593, A68
Fu, S. Y., Zhu, Z. P., Liu, X., et al. 2021, GCN, 29948
Fynbo, J. P. U., Izzo, L., de Ugarte Postigo, A., Malesani, D. B., & Pursimo, T.
    2021, GCN, 30182
Gal-Yam, A., Ofek, E. O., Poznanski, D., et al. 2006, ApJ, 639, 331
Gehrels, N., Chincarini, G., Giommi, P., et al. 2004, ApJ, 611, 1005
Ghosh, A., Dimple, Kumar, A., et al. 2021, GCN, 29364
Gimeno, G., Roth, K., Chiboucas, K., et al. 2016, Proc. SPIE, 9908, 99082S
Gordon, K. D., Clayton, G. C., Misselt, K. A., Landolt, A. U., & Wolff, M. J.
    2003, ApJ, 594, 279
Gottlieb, O., Nakar, E., & Bromberg, O. 2021, MNRAS, 500, 3511
Graham, M. J., Kulkarni, S. R., Bellm, E. C., et al. 2019, PASP, 131, 078001
Granot, J., Panaitescu, A., Kumar, P., & Woosley, S. E. 2002, ApJL,
    570, L61
Granot, J., & Ramirez-Ruiz, E. 2010, arXiv:1012.5101
Granot, J., & Sari, R. 2002, ApJ, 568, 820
Greiner, J., Hartmann, D. H., Voges, W., et al. 2000, A&A, 353, 998
Greiner, J., Krühler, T., Klose, S., et al. 2011, A&A, 526, A30
Grindlay, J. E. 1999, ApJ, 510, 710
Gruber, D., Goldstein, A., Weller von Ahlefeld, V., et al. 2014, ApJS, 211, 12
Guelbenzu, A. N., Rau, A., & Klose, S. 2021, GCN, 29330
Gupta, R., Kumar, A., Bhushan Pandey, S., et al. 2022, JApA, 43, 11
Gupta, R., Pandey, S. B., Kumar, A., et al. 2021, GCN, 29490
Gupta, S., Sharma, V., Bhattacharya, D., et al. 2020, GCN, 27818
Harrison, F. A., Yost, S. A., Sari, R., et al. 2001, ApJ, 559, 123

Heise, J., Zand, J. I., Kippen, R. M., & Woods, P. M. 2001, in Gamma-ray
    Bursts in the Afterglow Era, ed. E. Costa, F. Frontera, & J. Hjorth (Berlin:
    Springer), 16
Ho, A., Yao, Y., & Perley, D. 2021a, GCN, 29953
Ho, A. Y. Q., Kulkarni, S. R., Nugent, P. E., et al. 2018, ApJL, 854, L13
Ho, A. Y. Q., Perley, D. A., Yao, Y., & Andreoni, I. 2021b, TNSAN, 20, 1
Ho, A. Y. Q., Perley, D. A., Beniamini, P., et al. 2020a, ApJ, 905, 98
Ho, A. Y. Q., Perley, D. A., Kulkarni, S. R., et al. 2020b, ApJ, 895, 49
Ho, A. Y. Q., Yao, Y., Perley, D. A. & GROWTH Collaboration 2020c, GCN,
    25658
Ho, A. Y. Q., Perley, D. A., Gal-Yam, A., et al. 2021c, arXiv:2105.08811
Hook, I. M., Jørgensen, I., Allington-Smith, J. R., et al. 2004, PASP, 116, 425
Hosokawa, R., Nakamura, N., Murata, K. L., et al. 2020, GCN, 27824
Hu, Y. -D., Fernandez-Garcia, E., Castro-Tirado, A. J., et al. 2021, GCN,
    29312
Huang, Y. F., Dai, Z. G., & Lu, T. 2002, MNRAS, 332, 735
Huang, Y. F., Wu, X. F., Dai, Z. G., Ma, H. T., & Lu, T. 2004, ApJ, 605, 300
Huang, Y.-J., Urata, Y., Huang, K., et al. 2020, ApJ, 897, 69
Hunter, J. D. 2007, CSE, 9, 90
Hurley, K., Ipn, Mitrofanov, I. G., et al. 2021, GCN, 29408
Izzo, L. 2020, GCN, 27817
Kann, D. A., de Ugarte Postigo, A., Thoene, C. C., et al. 2021a, GCN, 29321
Kann, D. A., Klose, S., Zhang, B., et al. 2010, ApJ, 720, 1513
Kann, D. A., Klose, S., Zhang, B., et al. 2011, ApJ, 734, 96
Kann, D. A., Nicuesa Guelbenzu, A., de Ugarte Postigo, A., et al. 2021b, GCN,
    29344
Kasliwal, M. M., Anand, S., Ahumada, T., et al. 2020, ApJ, 905, 145
Kasliwal, M. M., Cannella, C., Bagdasaryan, A., et al. 2019, PASP, 131,
    038003
Kasliwal, M. M., Nakar, E., Singer, L. P., et al. 2017, Sci, 358, 1559
Kennea, J. A., Osborne, J. P., Page, K. L., et al. 2021, GCN, 29413
Khabibullin, I., Sazonov, S., & Sunyaev, R. 2012, MNRAS, 426, 1819
Kim, V., Pankov, N., Krugov, M., et al. 2021, GCN, 29950
Kool, E., Andreoni, I., Ho, A., et al. 2021, TNSAN, 54, 1
Kouveliotou, C., Wijers, R. A. M. J., & Woosley, S. 2012, Gamma-ray Bursts
    (Cambridge: Cambridge Univ. Press)
Krühler, T., Greiner, J., Afonso, P., et al. 2009, A&A, 508, 593
Kuin, N. P. M., Page, K. L. & Swift UVOT Team 2020, GCN, 27825
Kulkarni, S. R., Djorgovski, S. G., Odewahn, S. C., et al. 1999, Natur, 398, 389
Kumar, A., Pandey, S. B., Ghosh, A., et al. 2020a, GCN, 27806
Kumar, A., Pandey, S. B., Gupta, R., et al. 2021, GCN, 29308
Kumar, H., Bhalerao, V., Anupama, G. C., et al. 2020b, GCN, 27800
Kumar, P., & Zhang, B. 2015, PhR, 561, 1
Laskar, T., Alexander, K. D., Berger, E., et al. 2016, ApJ, 833, 88
Laskar, T., Alexander, K. D., Kilpatrick, C., et al. 2021, GCN, 30217
Laskar, T., Berger, E., Zauderer, B. A., et al. 2013, ApJ, 776, 119
Laskar, T., van Eerten, H., Schady, P., et al. 2019, ApJ, 884, 121
Law, C. J., Gaensler, B. M., Metzger, B. D., Ofek, E. O., & Sironi, L. 2018,
    ApJL, 866, L22
Law, N. M., Kulkarni, S. R., Dekany, R. G., et al. 2009, PASP, 121, 1395
Lei, W.-H., Zhang, B., & Liang, E.-W. 2013, ApJ, 765, 125
Levinson, A., Ofek, E. O., Waxman, E., & Gal-Yam, A. 2002, ApJ, 576, 923
Li, C. Y., Xiong, S. L., Xiao, S., et al. 2021, GCN, 29392
Li, L., Liang, E.-W., Tang, Q.-W., et al. 2012, ApJ, 758, 27
Lipunov, V., Gorbovskoy, E., Kornilov, V., et al. 2020, GCN, 27801
Lipunov, V., Kornilov, V., Gorbovskoy, E., et al. 2021, GCN, 29959
Littlejohns, O. M., Willingale, R., O'Brien, P. T., et al. 2012, MNRAS,
    421, 2692
Mahabal, A., Rebbapragada, U., Walters, R., et al. 2019, PASP, 131, 038002
Malacaria, C., Hristov, B., Fermi, G. B. M. & Fermi GBM Team 2021, GCN,
    30199
Margutti, R., Soderberg, A. M., Wieringa, M. H., et al. 2013, ApJ, 778, 18
Masci, F. J., Laher, R. R., Rusholme, B., et al. 2019, PASP, 131, 018003
McBreen, S., Krühler, T., Rau, A., et al. 2010, A&A, 516, A71
McKinney, J. C. 2006, MNRAS, 368, 1561
McKinney, W. 2010, in Proc. 9th Python in Science Conf., ed.
    S. van der Walt & J. Millman, 56
McMullin, J. P., Waters, B., Schiebel, D., Young, W., & Golap, K. 2007, in
    ASP Conf. Ser., 376, CASA Architecture and Applications, ed. R. A. Shaw,
    F. Hill, & D. J. Bell (San Francisco, CA: ASP), 127
Meegan, C., Lichti, G., Bhat, P. N., et al. 2009, ApJ, 702, 791
Melandri, A., Rossi, A., Benetti, S., et al. 2019, A&A, 621, A81
Mészáros, P. 2006, RPPh, 69, 2259
Mészáros, P., & Rees, M. J. 1997, ApJL, 482, L29
Mooley, K. P., Margalit, B., Law, C. J., et al. 2022, ApJ, 924, 16
Nakar, E., & Piran, T. 2003, NewA, 8, 141

Nakar, E., & Piran, T. 2017, ApJ, 834, 28
Nakar, E., Piran, T., & Granot, J. 2002, ApJ, 579, 699
Narayana Bhat, P., Meegan, C. A., von Kienlin, A., et al. 2016, ApJS, 223, 28
Nicuesa Guelbenzu, A., & Klose, S. 2021, GCN, 29528
Nysewander, M., Fruchter, A. S., & Pe'er, A. 2009, ApJ, 701, 824
O'Connor, B., Dichiara, S., Troja, E., et al. 2021, GCN, 29952
Ofek, E. O., & Ben-Ami, S. 2020, PASP, 132, 125004
Oke, J. B., Cohen, J. G., Carr, M., et al. 1995, PASP, 107, 375
Oke, J. B., & Gunn, J. E. 1983, ApJ, 266, 713
Paczyński, B. 1998, ApJL, 494, L45
Page, K. L., Gropp, J. D., Kennea, J. A., et al. 2021, GCN, 30170
Panaitescu, A., & Kumar, P. 2001, ApJL, 560, L49
Panaitescu, A., & Kumar, P. 2002, ApJ, 571, 779
pandas development team, T. 2020, pandas-dev/pandas: Pandas v1 5.0, Zenodo, doi:10.5281/zenodo.3509134
Pankov, N., Belkin, S., Klunko, E., et al. 2021a, GCN, 29954
Pankov, N., Pozanenko, A., Rumyantsev, V., Belkin, S., & GRB FuN, I. 2021b, GCN, 30245
Patterson, M. T., Bellm, E. C., Rusholme, B., et al. 2019, PASP, 131, 018001
Perley, D., Ho, A. & Zwicky Transient Facility Collaboration 2021a, GCN, 29508
Perley, D. A. 2019, PASP, 131, 084503
Perley, D. A., Cenko, S. B., Corsi, A., et al. 2014, ApJ, 781, 37
Perley, R. A., Chandler, C. J., Butler, B. J., & Wrobel, J. M. 2011, ApJL, 739, L1
Perley, D. A., Fremling, C., Sollerman, J., et al. 2020, ApJ, 904, 35
Perley, D. A., & Ho, A. 2020, GCN, 27805
Perley, D. A., Ho, A. Y. Q., Copperwheat, C. M. & Growth Collaboration 2019a, GCN, 25643
Perley, D. A., Ho, A. Y. Q., Yao, Y., et al. 2021b, MNRAS, 508, 5138
Perley, D. A., Ho, A. Y. Q., Yao, Y., & Perley, R. A. 2021c, GCN, 29343
Perley, D. A., Li, W., Chornock, R., et al. 2008, ApJ, 688, 470
Perley, D. A., Mazzali, P. A., Yan, L., et al. 2019b, MNRAS, 484, 1031
Perley, D. A., Yao, Y., Ho, A. Y. Q., et al. 2021d, GCN, 30206
Perna, R., & Loeb, A. 1998, ApJL, 509, L85
Piran, T. 2004, RvMP, 76, 1143
Planck Collaboration, Ade, P. A. R., Aghanim, P. A. R., et al. 2016, A&A, 594, A13
Pookalil, S., Mailyan, B., Hamburg, R. & Fermi GBM Team 2020, GCN, 27809
Poolakkil, S., Preece, R., Fletcher, C., et al. 2021, ApJ, 913, 60
Pozanenko, A., Belkin, S., Kim, V., et al. 2021, GCN, 29512
Prentice, S. J., Maguire, K., Smartt, S. J., et al. 2018, ApJL, 865, L3
Racusin, J. L., Oates, S. R., Schady, P., et al. 2011, ApJ, 738, 138
Ramirez-Ruiz, E., Celotti, A., & Rees, M. J. 2002, MNRAS, 337, 1349
Ramirez-Ruiz, E., Granot, J., Kouveliotou, C., et al. 2005, ApJL, 625, L91
Rau, A., Greiner, J., & Schwarz, R. 2006, A&A, 449, 79
Rhoads, J. E. 1997, ApJL, 487, L1
Rhoads, J. E. 1999, ApJ, 525, 737
Rhoads, J. E. 2003, ApJ, 591, 1097
Ricker, G. R., Atteia, J. L., Crew, G. B., et al. 2003, in AIP Conf. Ser. 662, Gamma-Ray Burst and Afterglow Astronomy 2001: A Workshop Celebrating the First Year of the HETE Mission, ed. G. R. Ricker & R. K. Vanderspek (Melville, NY: AIP), 3
Ricker, G. R., Winn, J. N., Vanderspek, R., et al. 2014, Proc. SPIE, 9143, 914320
Ridnaia, A., Svinkin, D., & Frederiks, D. 2020, JPhCS, 1697, 012030
Rigault, M., Neill, J. D., Blagorodnova, N., et al. 2019, A&A, 627, A115
Rossi, A., Melandri, A. & CIBO Collaboration 2021a, GCN, 29433
Rossi, A., Palazzi, E., Cusano, F. & Grawita Collaboration 2021b, GCN, 30079
Rossi, A., Palazzi, E. & Grawita Collaboration 2021c, GCN, 29327

Rumyantsev, V., Pozanenko, A., Belkin, S., et al. 2020, GCN, 27802
Ryan, G., van Eerten, H., MacFadyen, A., & Zhang, B.-B. 2015, ApJ, 799, 3
Sakamoto, T., Lamb, D. Q., Kawai, N., et al. 2005, ApJ, 629, 311
Sanwal, P., Misra, K., Ghosh, A., et al. 2020, GCN, 27803
Sari, R., Piran, T., & Halpern, J. P. 1999, ApJL, 519, L17
Sari, R., Piran, T., & Narayan, R. 1998, ApJL, 497, L17
Sarin, N., Hamburg, R., Burns, E., et al. 2022, MNRAS, 512, 1391
Shen, R., & Matzner, C. D. 2012, ApJ, 744, 36
Singer, L. P., Kasliwal, M. M., Cenko, S. B., et al. 2015, ApJ, 806, 52
Singh, K. P., Tandon, S. N., Agrawal, P. C., et al. 2014, Proc. SPIE, 9144, 91441S
Smith, I. A., Perley, D. A., & Tanvir, N. R. 2021, GCN, 30360
Soderberg, A. M., Nakar, E., Cenko, S. B., et al. 2007, ApJ, 661, 982
Stalder, B., Tonry, J., Smartt, S. J., et al. 2017, ApJ, 850, 149
Steele, I. A., Smith, R. J., Rees, P. C., et al. 2004, Proc. SPIE, 5489, 679
Svinkin, D., Golenetskii, S., Aptekar, R., et al. 2020, GCN, 27867
Svinkin, D., Golenetskii, S., Frederiks, D., et al. 2021a, GCN, 29511
Svinkin, D., Golenetskii, S., Frederiks, D., et al. 2021b, GCN, 29514
Tachibana, Y., & Miller, A. A. 2018, PASP, 130, 128001
Tchekhovskoy, A., McKinney, J. C., & Narayan, R. 2008, MNRAS, 388, 551
Teja, R. S., Dutta, A., Kumar, H., et al. 2021, GCN, 29414
Tonry, J. L., Denneau, L., Heinze, A. N., et al. 2018, PASP, 130, 064505
Totani, T., & Panaitescu, A. 2002, ApJ, 576, 120
Tsvetkova, A., Frederiks, D., Golenetskii, S., et al. 2017, ApJ, 850, 161
Tsvetkova, A., Frederiks, D., Svinkin, D., et al. 2021, ApJ, 908, 83
van der Walt, S., Crellin-Quick, A., & Bloom, J. 2019, JOSS, 4, 1247
van Eerten, H., Zhang, W., & MacFadyen, A. 2010, ApJ, 722, 235
van Paradijs, J., Kouveliotou, C., & Wijers, R. A. M. J. 2000, ARA&A, 38, 379
van Roestel, J., Bellm, E. C., Duev, D. A., et al. 2019, RNAAS, 3, 136
Vedrenne, G., Roques, J. P., Schönfelder, V., et al. 2003, A&A, 411, L63
Villar, V. A., Berger, E., Metzger, B. D., & Guillochon, J. 2017a, ApJ, 849, 70
Villar, V. A., Guillochon, J., Berger, E., et al. 2017b, ApJL, 851, L21
Virtanen, P., Gommers, R., Oliphant, T. E., et al. 2020, NatMe, 17, 261
von Kienlin, A. 2014, GCN, 16450
von Kienlin, A., Meegan, C. A., Paciesas, W. S., et al. 2020, ApJ, 893, 46
Wang, J., Zhu, Z. P., Xu, D., et al. 2018, ApJ, 867, 147
Waratkar, G., Shenoy, V., Vibhute, A., et al. 2021, GCN, 29410
Watson, A. M., Butler, N., Becerra, R. L., et al. 2021, GCN, 29940
Wei, J., Cordier, B., Antier, S., et al. 2016, arXiv:1610.06892
White, N. E., Bauer, F. E., Baumgartner, W., et al. 2021, Proc. SPIE, 11821, 1182109
Willingale, R., Starling, R. L. C., Beardmore, A. P., Tanvir, N. R., & O'Brien, P. T. 2013, MNRAS, 431, 394
Winkler, C., Courvoisier, T. J. L., Di Cocco, G., et al. 2003, A&A, 411, L1
Xu, D., Izzo, L., Fynbo, J. P. U., et al. 2021, GCN, 29432
Yao, Y., Ho, A. Y. Q., Medvedev, P., et al. 2022, ApJ, 934, 104
Yao, Y., Miller, A., Ho, A., & Perley, D. 2021a, GCN, 29673
Yao, Y., Miller, A. A., Kulkarni, S. R., et al. 2019, ApJ, 886, 152
Yao, Y., Perley, D., & Ho, A. 2021b, GCN, 29938
Yao, Y., Perley, D., Ho, A. & Zwicky Transient Facility Collaboration 2021c, GCN, 29508
Yaron, O., & Gal-Yam, A. 2012, PASP, 124, 668
Yuan, W., Zhang, C., Ling, Z., et al. 2018, Proc. SPIE, 10699, 1069925
Zackay, B., Ofek, E. O., & Gal-Yam, A. 2016, ApJ, 830, 27
Zeh, A., Klose, S., & Kann, D. A. 2006, ApJ, 637, 889
Zhang, D., Li, X., Xiong, S., et al. 2019, NIMPA, 921, 8
Zheng, W., Filippenko, A. V., & GRB Team, K. A. I. T. 2020, GCN, 27814
Zhang, W., Woosley, S. E., & Heger, A. 2004, ApJ, 608, 365
Zhu, Z. P., Fynbo, J. P. U., Perley, D. A., Fu, S. Y., & Xu, D. 2021, GCN, 29310